Review

Electronic and Transport Properties of Epitaxial Graphene on SiC and 3C-SiC/Si: A Review

Aiswarya Pradeepkumar [1], **D. Kurt Gaskill [2]** and **Francesca Iacopi [1,3,*]**

[1] Faculty of Engineering and IT, University of Technology Sydney, Sydney, New South Wales 2007, Australia; aiswarya.pradeepkumar@uts.edu.au

[2] Institute for Research in Electronics and Applied Physics, University of Maryland, College Park, MD 20742, USA; kurtcapt87@verizon.net

[3] ARC Centre of Excellence in Future Low-Energy Electronics Technologies, Faculty of Engineering and IT, University of Technology Sydney, Sydney, New South Wales 2007, Australia

* Correspondence: francesca.iacopi@uts.edu.au

Abstract: The electronic and transport properties of epitaxial graphene are dominated by the interactions the material makes with its surroundings. Based on the transport properties of epitaxial graphene on SiC and 3C-SiC/Si substrates reported in the literature, we emphasize that the graphene interfaces formed between the active material and its environment are of paramount importance, and how interface modifications enable the fine-tuning of the transport properties of graphene. This review provides a renewed attention on the understanding and engineering of epitaxial graphene interfaces for integrated electronics and photonics applications.

Keywords: epitaxial graphene; SiC; 3C-SiC on Si; substrate interaction; carrier concentration; mobility; intercalation; buffer layer; surface functionalization

1. Introduction

The properties of graphene as well as other members of the two-dimensional (2D) class of materials differ fundamentally from those of typical electronic materials, which makes this class very attractive for future device applications [1]. A particular appealing property of graphene and other 2D materials is the possibility of dynamically tuning their electrical/electronic properties.

Yet, no matter the application under consideration, which range from light detectors to signal modulators and switches, Hall standards, or chemical sensors, control of transport properties is paramount, and the achievement of the sought-after tunability is not always trivial. The very attractive physical nature of the class (i.e., the large surface to volume ratio [2]) is a double-edged sword as interfaces between the material and its surrounding environment, e.g., substrate, interfaces, adsorbents, and metallization, have a significant effect on conductivity [2–5]. Graphene and 2D materials are made out of surfaces. The accurate control of surfaces and interfaces has historically always been a critical and challenging aspect of semiconductor technology [6,7]. Hence, in order to harness the properties of graphene in electronics, a significant shift in the technological approach needs to be made.

In this review, we explore recent advancements made in the charge transport research on epitaxial graphene (EG) synthesized on SiC and Si substrates as these are necessary ingredients for technological applications. Yet, the properties of EG on these substrates are very different.

For EG on 6H-SiC(0001) (the so-called silicon-terminated surface, Si-face), silicon sublimation results in the formation of EG [8] and the properties are dominated by the $6\sqrt{3} \times 6\sqrt{3}$ rotated 30° reconstruction [9] of the SiC surface. The modification of this reconstruction at the interface after graphene synthesis, often termed the buffer layer, has a profound effect on EG conductivity. In addition,

for two or more layers, this reconstruction naturally leads to Bernal stacking [10,11]. For graphene on SiC(000$\bar{1}$) (aka the carbon-terminated, C-face), the surface reconstructs [9] as (1 × 1), which relaxes the stacking constraint and likely contributes to the observed rotational disorder of the layers [12] and weaker substrate interaction. Moreover, the enhanced Si sublimation rate at screw dislocations likely results in some non-uniformity of thickness [13]. The transport properties of these multilayer graphenes (sometimes termed multilayer epitaxial graphenes, MEG) are complex with at least three conduction channels present [14]. Yet, careful control of nucleation has resulted in one to two layers of EG on the C-face with more easily characterized properties [15].

For graphene on 3C-SiC films on Si surfaces, the synthesis route traditionally employs a modified sublimation approach [16–20] or, more recently, a precipitation method using a metal catalyst alloy with evidence pointing to an epitaxial ordering [21]. For the case of EG on 3C-SiC(100)/Si, no buffer layer is formed, but the current state-of-the-art results in interface oxidation/silicates, which contribute to the conductivity [21]. This is in contrast to EG on 3C-SiC(111)/Si, which does appear to form a buffer layer [17,21] with similarity to that of the buffer layer formed on SiC(0001). However, silicates formation at the EG/3C-SiC interface competes to determine the conductivity.

In the following sections, we begin with a discussion of some basic graphene properties, given in Section 2. The main transport measurements methods are discussed in Section 3. Section 4 provides a focus upon the properties of EG on the SiC and Si substrate components since these dominate the charge transport. Then, we discuss the impact of various situations that modify the conductivity of EG such as ambient adsorbents and metals contacts. Section 5 describes the fine-tuning of the impacts from various surrounding interactions via intercalation, functionalization, and gate control.

2. Electronic Band Structure

2.1. Monolayer Graphene

The electronic properties of graphene were first described by P.R. Wallace in 1947 [22] who used the nearest neighbour tight-binding model (involving only p_z electrons perpendicular to the plane of graphene, i.e., p_z orbitals—hich result in π bands) to approximate the low energy electronic structure of an infinite graphene lattice, which demonstrates the linear dispersion.

$$E(k) = \pm\tau \sqrt{1 + 4cos\left(\frac{\sqrt{3}}{2}ak_x\right)cos\left(\frac{1}{2}ak_y\right) + 4cos^2\left(\frac{1}{2}ak_y\right)} \tag{1}$$

The linear dispersion relation of electrons in single-layer graphene can be written using the strong-coupling approximation by taking into account only the nearest-neighbor interaction (low-energy approximation) as follows.

$$E(\Delta k) = crhv_F\,\Delta k \tag{2}$$

where ***crh*** is the reduced Planck's constant, the proportionality or slope is the Fermi velocity, v_F is approximately equal to 10^6 m s^{-1}, and Δk is the momentum relative to the K points of the hexagonal reciprocal unit cell [23]. The band structure of a monolayer graphene (MLG), shown in Figure 1, exhibits the gapless linear dispersion (in k-space known as the Dirac cone) of the π bands at the K-point. This has two important implications. The first is the charge carriers, Dirac fermions, which are massless. The second is semi-metallic behaviour [22,24] because when the Fermi energy, E_F, is located where the dispersion converges to a point (the Dirac point, E_D), the density of states is zero, and electronic conduction is possible only through thermally excited electrons [25]. The linear dispersion of monolayer graphene results in several extraordinary electronic properties such as an anomalous quantum Hall effect with Berry's phase of π [8,26–29].
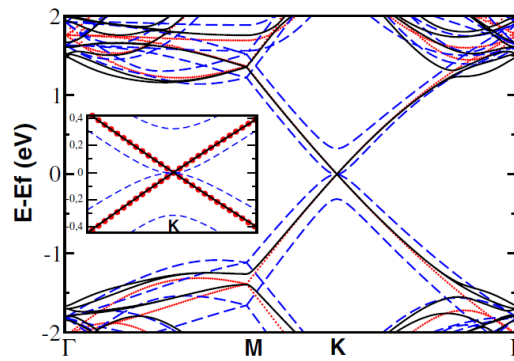
Figure 1. Band structure for a monolayer graphene (dotted line), a bilayer graphene with AB stacking (dashed line), and R30/R2$^+$ rotational fault pair (single line). Band structure at the *K*-point is given in the inset. Reprinted with permission from Reference [23]. Copyright (2008) by American Physical Society.

The tight-binding model oversimplifies the situation of EG on SiC(0001) as a buffer layer exists between SiC and EG. Mattausch and Pankratov [30] and Varchon et al. [31] performed a first-principles calculation, which included the buffer layer and determined the E_F was about 450 meV above the E_D due to doping of the graphene layer by charge transfer from the buffer layer. This is in agreement with angle-resolved photoelectron spectroscopy (ARPES) measurements [26,32–34]. Sprinkle et al. [35] found the average Fermi velocity, obtained from the slope of $E(\Delta k)$ as $v_F = 1.0$ (± 0.05) $\times 10^6$ ms^{-1} for energies down to ~500 meV above E_D [19,36,37]. This value of v_F is larger than the v_F for bulk graphite ($v_F = 0.86 \times 10^6$ ms^{-1}) [38].

Ouerghi et al. measured the band structure of the monolayer EG/3C-SiC(111) using ARPES at room temperature [19] (see Figure 2) and found the E_F. Using the linear dispersion, the charge carrier concentration, *n*, of monolayer graphene can be obtained as:

$$n = (E_F - E_D)^2/(\pi)(h v_F)^2 \tag{3}$$

where *h* is the Planck's constant, $v_F = 1.1 \times 10^6$ m s^{-1}, and E_F is 500 meV. This resulted in $n \sim 2 \times 10^{13}$ cm^{-2}.
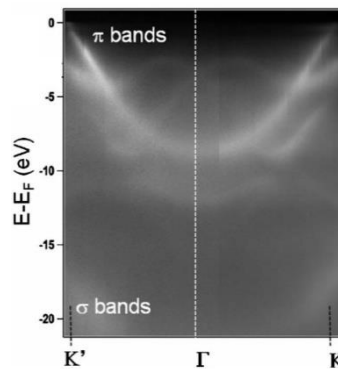

Figure 2. Electronic structure of monolayer EG on 3C-SiC(111) by ARPES. Reprinted with permission from Reference [19]. Copyright (2010) by American Physical Society.

The influence of graphene-substrate interaction on v_F of monolayer epitaxial graphene was estimated by Davydov [39] in which the substrate interaction reduces the v_F of electrons.

2.2. Bilayer Graphene

Bilayer graphene (BLG) synthesized on SiC(0001) are generally reported to be AB (Bernal) stacked with a 30° rotation with respect to the substrate [11]. In BLG, the charge carriers tunnel quantum

mechanically between the two layers, which causes a band dispersion that is nearly parabolic [40] (Figure 1) with an effective mass (m^*) of about 0.033 m_e (electron mass) [41].

$$E_{k\pm} = \pm v_F^2 k^2 t^{-1} \tag{4}$$

$E_{k\pm}$ describes the two bands with energies E_+ and E_- that lies at the K point, $t \sim 3$ eV is the energy of electron transition between the nearest neighbors spaced by a = 0.142 nm (lattice constant).

In this case, the v_F depends on the Fermi momentum (p_F) divided by m^* as p_F/m^* [42]. For higher energies corresponding to doping above 5×10^{12} cm^{-2}, the linear dependence is a good approximation [41]. Ohta et al. performed an early investigation of the band structure properties of BLG on SiC(0001) using ARPES, and found E_F to be 400 meV [34]. De Heer et al. reports v_F to be 0.7–0.8 $\times 10^6$ ms^{-1} for BLG, which is 20% to 30% smaller than that of MLG with an E_F at ~300 meV above the Dirac point [31]. However, recent measurements put v_F of MLG closer to 1.2×10^6 ms^{-1} [43] with an E_F of ~350 meV. Bernal stacked layers exhibit Berry's phase of 2π [40] as confirmed by the quantum Hall effect [44].

Charge transport in BLG, thus, involves massive chiral and parabolic dispersion carriers [42] (see Figure 1 with a zero band gap). The effect of the buffer layer is not included in contrast to the massless chiral, linear-dispersion carrier system for MLG.

The band structure of BLG is sensitive to the lattice symmetry [34]. When the graphene layers of a BLG are made asymmetric, a band gap forms between the low-energy bands at the former Dirac point [34,40] (see Figure 3). This means the band gap can be varied by means of an external transverse electrical field to control the density of electrons. The gap can be varied from 0 to 0.3 eV by changing the doping level between the two layers or by an external gate control [34,45]. Thus, the BLG transitions from a semi-metal to an insulator [34]. An externally controlled symmetry breaking also changes the electronic conductivity and forms a BLG switch [34]. For this reason, digital electronic applications have been envisioned [25].
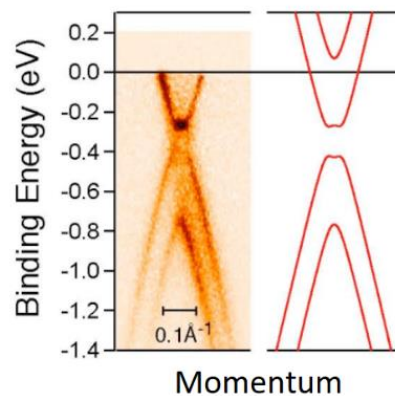

Figure 3. Band structure of BLG on SiC(0001) from ARPES and theoretical (solid lines). Reprinted with permission from Reference [34]. Copyright (2006) American Association for the Advancement of Science.

2.3. Turbostratic Multilayer Graphene

Turbostratic multilayer graphene layers are rotationally disordered and, thus, electrically decoupled. Epitaxial graphene formed on SiC(000$\bar{1}$) by thermal decomposition on both (0001) and SiC(000$\bar{1}$) by solid-phase epitaxy and on 3C-SiC/Si via the alloy mediated graphitization is reported to be turbostratic [21,46,47]. The rotational disorder in EG/SiC(000$\bar{1}$) was shown by low-energy electron diffraction (LEED) investigations in which an azimuthal diffraction pattern was found, and the strong intensity modulation in the bands denoted the rotational orientation [10,12,48]. In the case of EG/3C-SiC, the presence of turbostratic in-plane modes in the Raman spectroscopy indicated the rotational disorder [21]. With rotational disorder, the linear dispersion is recovered in the vicinity of

the K-points. The ab initio calculations show that the dispersion is nearly identical to that of an isolated MLG linear dispersion (see Figure 1), and predicts v_F to be the same as that of MLG [12,22,31].

Sprinkle et al. measured the linear dispersion using ARPES, as shown in Figure 4 [35]. In the ARPES data, the linear dispersions of adjacent decoupled layers can be readily seen as well as the n-type conductivity, where E_F is as low as ~14 meV, and the carrier density is ~10^{11} cm^{-2}. Furthermore, the v_F of MLG is close to the v_F of MEG formed by thermal decomposition of the SiC(000$\bar{1}$) obtained from infra-red measurements (1.02 ($\pm$0.01) $\times$ 10^6 ms^{-1}) [49] and scanning tunneling spectroscopy (1.07 ($\pm$0.01) $\times$ 10^6 ms^{-1}) [50].
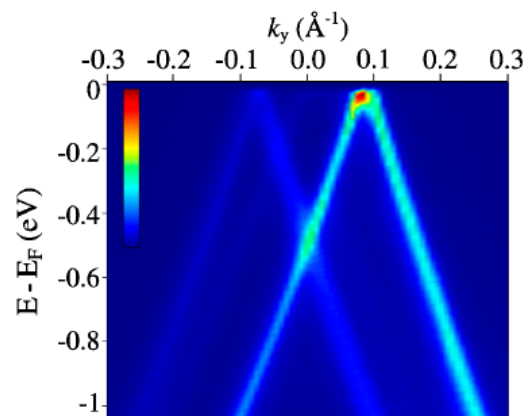

Figure 4. Band structure of EG on (000$\bar{1}$) 6H-SiC with 11 epi-layers obtained from ARPES. Two linear Dirac cones are observed. Reprinted with permission from Reference [35]. Copyright (2009) by American Physical Society.

In the next sections, we will discuss the electronic and transport properties of EG on SiC and 3C-SiC substrates with respect to the substrate, ambient, and metal contact interactions. Section 3 will discuss the different measurement methods used for the charge carrier transport study.

3. Transport Measurement Methods

Knowledge of the transport properties of graphene such as sheet carrier concentration, mobility, and sheet resistance and the factors affecting them are crucial for any applications of the graphene into practical devices. These include Hall effect measurements using Hall bar devices and van der Pauw (vdP) structures, Field-effect measurements using gated devices, Raman spectroscopy (carrier concentration from G peak shift), and ARPES (discussed in Section 2.1).

3.1. Hall Bar Devices

The first transport measurements were performed using Hall bar structures patterned on 6H-SiC(0001) by Berger et al. [4]. In this case, low mobility values were obtained in most of the samples, which may have been limited by the substrate step edges. Yet, the samples clearly demonstrated 2D electron gas properties and most of the important transport features of epitaxial graphene [4].

At the step edges, a second graphene layer is often formed, which is associated with step bunching and results in non-uniform graphene thickness [17] and unreliable transport measurement results [51]. S-H Ji et al. demonstrated that a strong impact of substrate steps degrades the transport properties of epitaxial graphene on SiC using scanning tunneling microscopy-based localized transport measurements [51]. Yakes et al. reported somewhat similar results noting that conductivity anisotropy in graphene was associated with substrate steps. The observed results were explained using a model where a charge build-up at the substrate steps leads to scattering [52]. For these reasons, Hall bar structures are often patterned to be parallel or perpendicular to steps (see Figure 5) to mitigate the effects of steps, and this approach was used for quantum Hall effect [53] devices. We note that Kruskopf

and co-workers developed an approach to form EG on SiC(0001) that is essentially free of steps [54] and demonstrated excellent quantum Hall effect results.
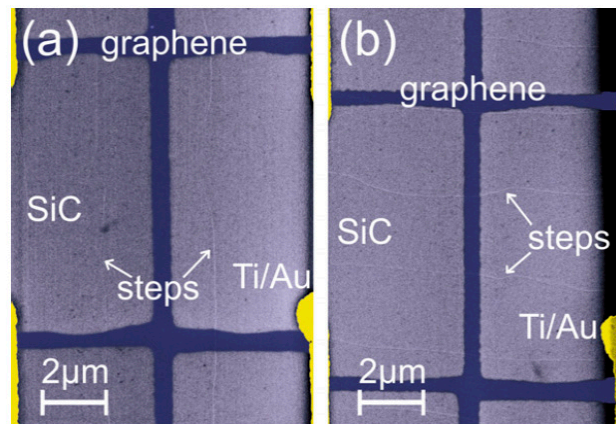

Figure 5. Scanning electron microscopy images of Hall bars fabricated on MLG (**a**) on a flat terrace and (**b**) perpendicular to the step edges on 6H-SiC. Reprinted with permission from Reference [55]. Copyright (2011) Elsevier Ltd.

3.2. Van der Pauw and Hall Bar Structures

Transport measurements from the van der Pauw method deliver large scale measurements [21,55,56] and provide complete information on carrier transport in EG. vdP and Hall bar-based measurements are limited by thickness inhomogeneities and discontinuities in the epitaxial films [21,57]. Jobst et al. demonstrated that the transport properties obtained from Hall bar measurements are almost the same as those from van der Pauw measurements, as shown in Figure 6 [55].
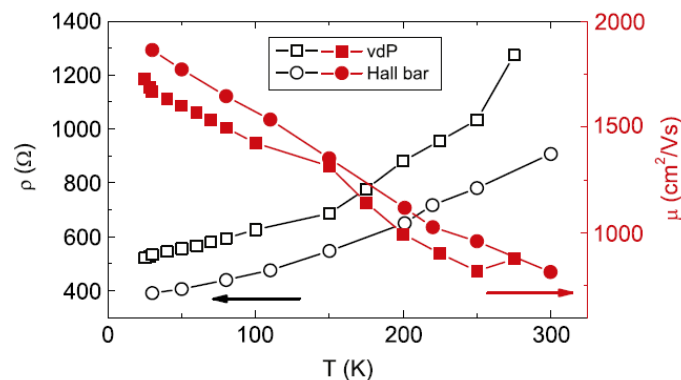

Figure 6. Resistivity, ρ, and mobility, μ, as a function of temperature, T for MLG on SiC, indicating that the measured properties are almost similar for vdP (squares) and Hall bar (circles) structures. Reprinted with permission from Reference [55]. Copyright (2011) Elsevier Ltd.

3.3. Field-Effect Measurements

The electric field-effect from an externally applied voltage to a gate enables the study of the extraordinary electrical properties of graphene [29,58]. The first observation of the electric field-effect in graphene (using mechanically exfoliated graphene onto SiO_2/Si) was reported by K.S. Novoselov and A.K. Geim [29], where the charge transport was switched between electron and hole gases via the gate voltage. Berger et al. performed the first transport studies of EG on SiC(0001) and modulated the electron density via electrostatic gating, which demonstrated the 2D electron gas properties [4]. The deleterious anisotropy effects of step bunching on SiC(0001) on gated devices has been discussed by Lin et al. [59]. In the case of graphene on SiC(000$\bar{1}$), the non-uniform thickness limits gate device applications [60].

In addition, the transport properties from field-effect measurement are dependent on geometry and electrostatics and are affected by the substrate [61]. This transport measurement method does not permit a systematic analysis of charge scattering within the system [21].

3.4. Raman Spectroscopy

The values of phonon frequencies of EG on SiC depend on the mechanical strain and charge transfer between SiC and graphene [62]. The Raman G-band and the 2D band involve phonons at the $K + \Delta K$ points in the Brillouin zone [62–64]. The influence of the doping on the Raman bands has been studied by Das et al. [65] and Rohrl et al. [62] using a gate voltage controlled graphene transferred onto SiO_2/Si. G-peak frequency showed an upshift up to 20 cm^{-1} when the graphene is n-type doped at 4×10^{13} cm^{-2}. The influence of doping on the 2D-peak shift was shown to be weak and is ~10–30% compared to the G-peak shift (3–5 cm^{-1}) [66] (see Figure 7). The value of 2D to G peak intensity was determined by the carrier concentration [65] and indicates the graphene doping level. Mueller et al. [67] reported a method to extract the value of doping from the Raman G and 2D modes of graphene formed on any arbitrary substrates. Furthermore, Verhagen et al. [68] estimated the temperature dependent doping of monolayer and bilayer graphene on SiO_2/Si using Raman spectral mapping between 10 K and 300 K. More recently, in Reference [69], Shtepliuk et al. estimated the thickness dependent electron doping of EG/SiC by silver films from the red-shift and broadening of the 2D band. The same research group studied the temperature and time dependency of the H-intercalation on the p-type doping of quasi-free standing monolayer graphene on EG/SiC via micro-Raman spectroscopy in Reference [70].
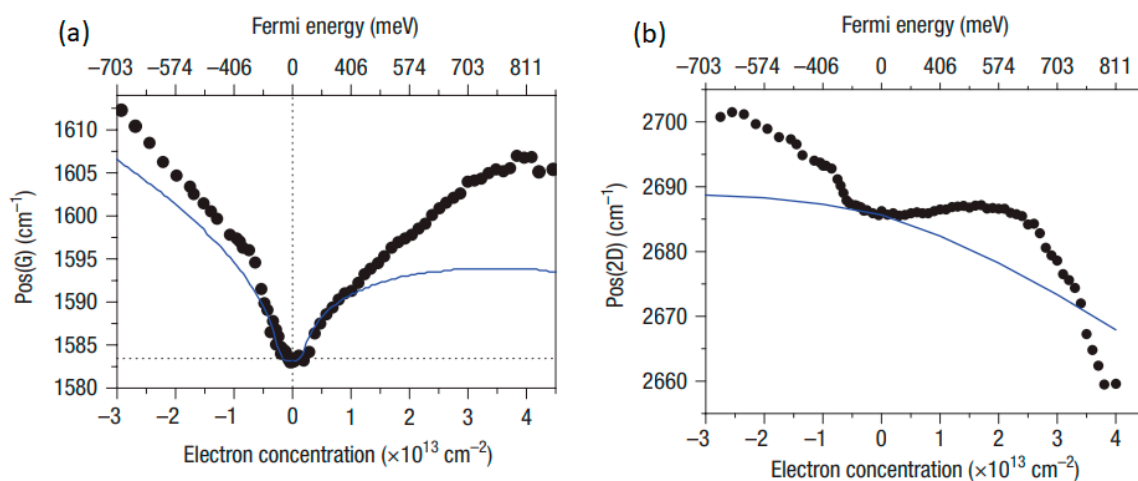

Figure 7. Position of the (**a**) G peak and (**b**) 2D peak as a function of electron and hole doping in graphene on SiO_2. The solid blue line in (**a**) is the predicted non-adiabatic trend from Reference [71]. The solid line in (**b**) is from density functional theory calculation. Reprinted with permission from Reference [65]. Copyright (2008) Springer Nature.

4. Electronic and Transport Properties: Effect of Interactions with the Surroundings

Table 1 shows a summary of electronic and transport properties of as-grown EG on SiC(0001), SiC(000$\bar{1}$), and 3C-SiC/Si substrates showing the effect of EG-substrate and EG-ambient interactions as well as the properties fine-tuned via intercalation, functionalization, and gate control. These properties are discussed throughout the following sections.

Table 1. Summary of electronic and transport properties of as-grown epitaxial graphene on SiC(0001), SiC(000$\bar{1}$), and 3C-SiC/Si substrates indicating the effect of substrate and ambient and fine-tuning of properties using intercalation, functionalization, and gate control.

Substrate	Growth Process	No. of EG Layers	Fermi Level, E_F (meV)	n/p	n (cm^{-2})	μ (cm$^2 \cdot$V$^{-1} \cdot$s^{-1})	R_{sh} ($\Omega/\square$)	Measurement Technique	Reference
					Transport Properties at 300 K				**Reference**
					EG-Substrate Interaction				
6H-SiC(0001)	Thermal decomposition	1	350–500	n	10^{13}	1000	-	Hall bar	[26,43]
6H-SiC(0001)	Thermal decomposition	2	300–400	n	5×10^{12}	1000	-	Hall bar	[31,34]
6H-/4H-SiC(0001)	Thermal decomposition	Multi	-	n/p	10^{13}–10^{14}	1000–3000		Hall bar	[56]
6H-/4H-SiC(000$\bar{1}$)	Thermal decomposition	Multi (top) (mid) (first)	-	p p n	2×10^{13} 5×10^{11} 2×10^{13}	1500 19,300 12,400	-	Hall bar	[14]
4H-SiC(000$\bar{1}$)	Thermal decomposition	First layer	350	n	9×10^{12}	~1500	-	Optical Hall effect	[72,73]
4H-SiC(000$\bar{1}$)	Thermal decomposition	Multi	-	p	10^{12}	15,000	-	Hall bar	[15]
3C-SiC(100) 3C-SiC(111)	Alloy mediated	3–7	450	p	3×10^{13} 10^{12}	<80 330	~10k	vdP	[21]
					EG-Ambient Interaction				
4H-SiC(0001)	Thermal decomposition	1		p	10^{12}	~1550	-	Optical Hall effect	[74]
					Fine-Tuning of Transport Properties				
					H-Intercalation				
4H-SiC(0001) 6H-SiC(0001)	Thermal decomposition	Quasi-free-standing monolayer	340 300	p	9×10^{12} 6×10^{12}	-	-	ARPES	[75]

Table 1. *Cont.*

Substrate	Growth Process	No. of EG Layers	Transport Properties at 300 K						Reference
			Fermi Level, E_F (meV)	n/p	n (cm^{-2})	μ (cm$^2\cdot$V$^{-1}\cdot$s^{-1})	R_{sh} (Ω/□)	Measurement Technique	
3C-SiC(111)	Thermal decomposition	Quasi-free-standing monolayer	-	n	10^{12}	-	-	APRES	[76]
6H-SiC(0001)	Thermal decomposition	Quasi-free-standing bilayer	230	p	10^{12}	-	-	APRES	[77]
3C-SiC(111)	Alloy mediated	3–7	320	p	3×10^{12}	350	6k	vdP, density functional theory	[21]
Oxygen Intercalation									
6H-SiC(0001)	Thermal decomposition	1	300 200	n	5×10^{12} 2×10^{12}	-	-	ARPES (partial intercalation)	[78]
Magnesium Intercalation									
6H-SiC(0001)	Thermal decomposition	Quasi-free-standing bilayer	720	n	2×10^{14}	-	-	APRES, density functional theory	[43]
Functionalization									
F4-TCNQ/Si-face SiC	Thermal decomposition	1	10	n	5×10^{10}	29000	-	Hall bar (25 K)	[55,79]
Top-gate Graphene Field-Effect Transistor									
SiC(000$\bar{1}$) SiC(000$\bar{1}$)	Thermal decomposition	Multilayer	-	n/p		600–1200 (0001) 500–3000 (000$\bar{1}$)	-	Field-effect transistor	[60]
3C-SiC(111)/Si(111)	Thermal decomposition	-	-	n/p	-	175 (n) 285 (p)	-	Field-effect transistor	[80]

4.1. Epitaxial Graphene-Substrate Interaction

4.1.1. Induced Pseudo-Charge Due to Substrate Polarization Effect

As described by the ARPES results summarized in Section 2, EG on SiC(0001) exhibits an E_F is quite large, which indicates considerable n-type doping. Although some density functional theory (DFT) calculations imply this result, the physical reasons have been clarified by the experimental work of Ristein et al. and Mammadov et al. [75,81]. The doping originates from three effects and, in some cases, existing simultaneously: (i) polarization induced pseudo-charge due to the hexagonal nature of 6H-SiC and 4H-SiC substrates, (ii) surface states associated with C and Si dangling bonds overlaid on the broad density of states (DOS) of the buffer layer, which act as donor states (part of the Kopylov model [82]), and (iii) the effect of space-charge layer in (doped) SiC or Si substrates due to band bending at the interface. Figure 8 illustrates these effects. The referenced works [75,81] demonstrate these reasons are in reasonable agreement with the experiment, especially for hydrogen intercalated graphene (see Section 5.1).
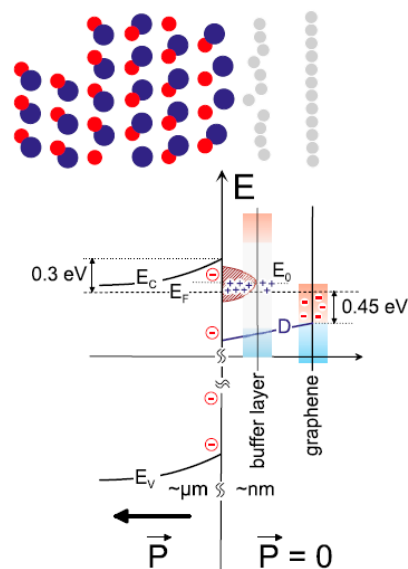

Figure 8. Sketch and band diagram for monolayer EG on SiC(0001). Blue and red circles indicate Si and C atoms, respectively. The polarization is shown at the bottom. The negative polarization related to the discontinuity of the interface polarization is a pseudo charge (marked in circles). D indicates the electrostatic potential between the EG and SiC. The band bending details have been taken from Reference [83]. Adapted with permission from Reference [81]. Copyright (2012) American Physical Society.

The implications of this understanding are significant. (1) Preparing EG on a defect-free interface of SiC ($000\bar{1}$) should result in n-type doping. (2) EG on 3C-SiC should lead to n-doped graphene layers—modified only by the induced effects of substrate donor states. (3) Varying the hexagonality of the substrate will change the doping. This has been successfully tested using 4H-SiC and 6H-SiC [75].

The spontaneous polarization has been reported as a bulk property of hexagonal semiconductor compounds, which leads to a polarization charge on the polar surface of SiC, independent to any interface formation [75,81]. This is induced at the inversion of the stacking sequence of the hexagonal double layers while it is absent in the 3C-SiC polytype due to the symmetry [75]. The spontaneous polarization generates a pseudo acceptor layer with a pseudo charge density (Figure 8) depending on the hexagonal polytype [75]. Ristein et al. demonstrated that the sign and magnitude of SiC polarization agree with the charge concentration of H-intercalated graphene on SiC(0001) [81]. The hexagonality of the SiC affects the polarization proportionally, i.e., for the 4H-SiC(0001) the polarization is 6/4 times

larger than that for the 6H-SiC(0001) [75,81] and, as mentioned above, has been shown experimentally via the H-intercalation (Section 5.1).

4.1.2. Impact of Growth on SiC (0001)

Thermal decomposition of SiC in vacuum or argon atmosphere is the well-established process for producing graphene on SiC [5,56,75,84]. Electronic and transport properties of EG on SiC depends upon the type of surface termination of SiC (Si-face or C-face). Although both Si and C sublimate, the Si flux is dominant. The differences between the graphitic layer grown on the Si-face (0001) and the C-face (000$\bar{1}$) were first reported by Bommel et al. [85]

Graphene grown on SiC(0001) possesses a carbon-rich amorphous interfacial layer ($6\sqrt{3} \times 6\sqrt{3}$) rotated 30° [86] known as the buffer layer in between the SiC and graphene [31]. The buffer layer forms strong covalent bonds with the SiC. The electronic structure of the buffer layer shows a large gap and an E_F pinned by a state with a small dispersion close to the conduction band (see Figure 9) [31]. These states are related to the dangling bonds in the buffer layer. When more than one carbon layer is present, the graphene-related dispersions are recovered.
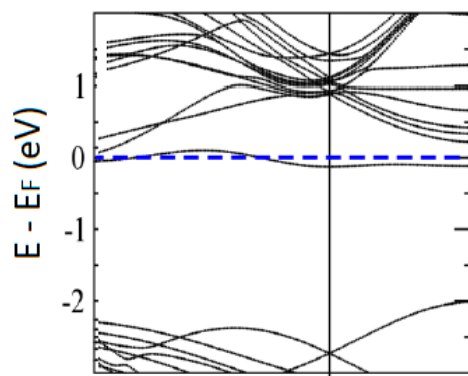

Figure 9. Dispersion curves for a buffer layer. Adapted with permission from Reference [31]. Copyright (2007) American Physical Society.

Emtsev et al. used ARPES measurements to study the band structure changes starting from the $6\sqrt{3}$ surface of SiC. The interaction of the buffer layer with the $6\sqrt{3}$ surface results in a σ-band instead of a π-band. Continued sublimation converts the buffer layer into graphene with π-band [86] and simultaneously creates a new buffer layer underneath. As-grown MLG on Si-face SiC is generally reported to be electron-doped with a carrier concentration of ~1×10^{13} cm^{-2} [26,37,82], 300 K mobility of ~1000 cm$^2 \cdot$V$^{-1} \cdot$s^{-1}, and a 25 K mobility of ~2000 cm$^2 \cdot$V$^{-1} \cdot$s^{-1} [26] [55]. The n-type conductivity is due to the charge transfer from donor-like states at the EG/SiC interface, i.e., the buffer layer, that overcompensates the spontaneous polarization of SiC [81], as discussed in Section 4.1.1.

The band structure for BLG on SiC(0001) was calculated using DFT by Varchon et al. [31] and is in agreement with the ARPES results by Ohta et al. [33,34]. Additional details are in Section 2.2. The E_F is ~250–400 meV above the Dirac point (n-type conductivity), which is slightly lower than that for epitaxial monolayers. This is likely due to charge transfer from the buffer layer [31], whose cause likely has some similarity with the effects discussed in Section 4.1.1. The carrier concentration $\approx 5 \times 10^{12}$ cm^{-2} [65] and the mobility is ~1000 cm$^2 \cdot$V$^{-1} \cdot$s^{-1} [45]. The lower E_F and doping level of BLG may indicate a weaker substrate interaction as reported by Ohta et al. [34]

4.1.3. Impact of Growth on SiC (000$\bar{1}$)

Unlike the graphene on SiC (0001), graphene formation on SiC (000$\bar{1}$) does not involve a buffer layer at the EG-SiC interface. This is because a different surface reconstruction occurs. Seurbet et al. [87] analyzed the atomic structure of the (2 × 2) reconstruction on (000$\bar{1}$) SiC using an in situ prepared

samples and quantitative LEED intensity analysis. In this case, $\frac{3}{4}$ of the carbon atoms on the $(000\bar{1})$ surface plane are bonded to a silicon adatom in a hollow site with two dangling bonds (Si adatom and C rest atom) [5].

　　Using first-principles, Varchon et al. calculated the band structure incorporating the (2×2) surface reconstruction (see Figure 10a) [5] and claimed that the electronegativity difference between silicon and carbon induces a charge transfer from the Si adatom to the C rest atom that forms surface states in the electronic band structure EG on $SiC(000\bar{1})$ (see Figure 10b) [31]. This results in pinning of the Fermi energy, which makes the samples n-type. Yet, Ristein et al. and Mammadov et al. argue the situation is more complex due to the hexagonal nature of the substrate (see Section 4.1.1) even though n-type behaviour is still predicted. This situation is clarified by detailed experimental work, which will be described below.
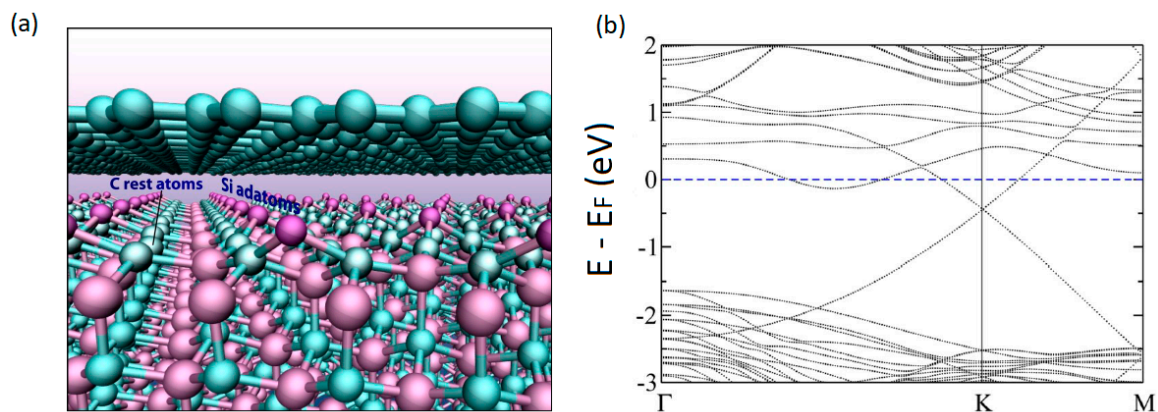

Figure 10. (**a**) EG/SiC$(000\bar{1})$ interface with the (2×2) C surface reconstruction. Si adatoms and C rest atoms are marked. Adapted with permission from Reference [5]. Copyright (2012) AIP Publishing. (**b**) Electronic band structure of EG on SiC$(000\bar{1}$). Adapted with permission from Reference [31]. Copyright (2007) American Physical Society.

　　The graphene layers on the C-face are thicker and randomly rotated against each other as well as with respect to the substrate [86,88] and, thus, exhibit weaker interactions with the substrate [48,86]. This unusual rotational stacking causes multilayers of graphene on the C-face to have an electronic structure similar to that of the monolayer graphene [8,35,88] with a well-defined Dirac cone (linear dispersion) near the charge neutrality point [22]. Shubnikov-de Haas oscillations were observed using Hall bars, which indicated that the transport layer has a Berry phase of π, similar to that of a single layer graphene. This signified that it is electronically decoupled from the layer above it [89]. Additional evidence for the decoupling is found in ARPES data of the multilayer EG (MEG) stack, which reveals the decoupled nature of the layers [35,48] in contrast to ARPES results on Bernal BLG on Si-face, where Dirac cones remain unperturbed and distinct from one another [90]. Infrared spectroscopy measurements shows E_F ~8 meV, doping ~10^{10} cm^{-2}, and low magnetic field mobility ~10^6 cm$^2 \cdot$V$^{-1} \cdot$s^{-1} [91].

　　Room temperature transport measurements reported on these MEG on C-face SiC samples are typically p-type [5] with sheet density of ~10^{13}–10^{14} cm^{-2} and mobility of ~1000–3000 cm$^2 \cdot$V$^{-1} \cdot$s^{-1} even though a wide range of values and even n-type measurements have been reported [14,56,72–74,92]. This seems to run counter to the n-type predictions noted in Section 4.1.1, which we will address next.

　　This difficulty of measured p-type properties vs. the n-type prediction situation is explained by considering the work of Lin et al. [14] who performed variable magnetic field Hall measurements on a series of samples. The data was best fit to a model where three types of transport regions exist in the layers of the sample: the layers closest to the substrate (substrate interaction), the interior layers (nearly neutral), and then the outer layers (ambient interaction). Each region has distinct sheet density and mobility. The epitaxial layer that lies closest to the SiC is highly electron-doped with high conductivity

(10^{12} cm^{-2}, 12,400 cm$^2 \cdot$V$^{-1} \cdot$s^{-1}). This is consistent with the models of Ristein and Mammadov [75,81]. The model is also supported by an ultrafast optical spectroscopy measurement that resulted in a doping density of 9×10^{12} cm^{-2} corresponding to a Fermi level of ~350 meV above the Dirac point for the layer close to the substrate [72].

The second transport region is nearly intrinsic (p-type, 5×10^{11} cm^{-2}, 20,000 cm$^2 \cdot$V$^{-1} \cdot$s^{-1}) due to charge screening. Additional support for this can be found, for example, from Landau level spectroscopy where the results are expected to be dominated by sample regions having high mobility [90]. Measurements of MEG have resulted in exceptionally high room temperature mobilities (>200,000 cm$^2 \cdot$V$^{-1} \cdot$s^{-1}) consistent with nearly intrinsic doping [48,50,93,94].

The third transport region is the heavily p-doped outermost layers (10^{13} cm^{-2}, 1500 cm$^2 \cdot$V$^{-1} \cdot$s^{-1}) likely due to environmental dopants [14] related to the ambient temperature [90]. Sidorov et al. determined that the environmental factors cause a p-type behaviour in ambient exposed monolayer and multilayer EG on SiC(000$\bar{1}$) [5] (a detailed discussion on the influence of ambient temperature on the transport of EG is given in Section 4.2). Lebedev et al. remarked that the outer layers of graphene, which are p-type, play a protecting role for the interior graphene layers, preventing influence from the atmosphere [92]. Sidorov et al. also reported that the natural conductivity state of MEG without the influence of ambient is n-type [5,84], which is also consistent with the substrate hexagonality argument. The difficulty in understanding the range of doping types reported by others is clarified by Lin since many samples analyzed using a simple one-layer model will tend to be p-type even though n-type results can occur depending upon overall thickness and uniformity. Hence, the variations in reported results are likely due to researchers assuming a simple model of uniform charge density and mobility when analyzing Hall data coupled with sample-to-sample variability.

A significant advancement in the transport of EG on 4H-SiC(000$\bar{1}$) was achieved when Wu et al. [15] synthesized a monolayer EG on the C-face, which was p-doped ~1.27×10^{12} cm^{-2} (likely due to environmental doping) with mobility of 20,000 cm$^2 \cdot$V$^{-1} \cdot$s^{-1} at 4 K and ~15,000 cm$^2 \cdot$V$^{-1} \cdot$s^{-1} at 300 K [95]. The same group has also demonstrated that the scattering effects due to the substrate (i.e., charge impurity, electron-phonon) are weak. This is related to the absence of a buffer layer, a weak EG-substrate interaction, and no induced charges into the graphene or scattering centres [56,96]. The values of MLG on 4H-SiC(000$\bar{1}$) are an order of magnitude larger than MLG on SiC(0001) and are in line with the values from exfoliated graphene on SiO$_2$ [97,98], even though later studies reported two-fold larger mobility of ~10^6 cm$^2 \cdot$V$^{-1} \cdot$s^{-1} at a carrier concentration of ~10^8 cm^{-2} and E_F within 1 meV for suspended graphene devices [99–101].

4.1.4. Impact of Growth on (100) and (111) 3C-SiC/Si

Synthesis of EG on Si substrates received attention primarily due to its compatibility with current micromachining technology and processes, low production cost, and ability to synthesize on large areas of substrates [21,66]. Thermal decomposition of 3C-SiC was widely adopted to form graphene on silicon substrates using 3C-SiC(111) and 3C-SiC(100) pseudo-substrates [16,18,20,66,80]. Yet, the formation EG on 3C-SiC via thermal decomposition has a limitation of inconsistent graphene coverage [102]. Pradeepkumar et al. [21] have overcome the coverage issue of graphene on 3C-SiC by using a liquid-phase Ni/Cu alloy-mediated graphene synthesis approach.

Similar to EG formed on SiC(0001), graphitization of (111) type 3C-SiC involves a buffer layer at the EG/3C-SiC interface [18]. Figure 11 shows the presence of the buffer layer in EG/3C-SiC(111) using X-ray photoelectron spectroscopy (XPS) measurements [21], which is also demonstrated in References [103] and [17]. The existence of the buffer layer in the EG/3C-SiC(111) substrate has also been proven by the transmission electron microscopy (TEM) measurements by Fukidome et al. [104]. Figure 11 also indicates that the EG formed on 3C-SiC(100) does not possess a buffer layer [21].
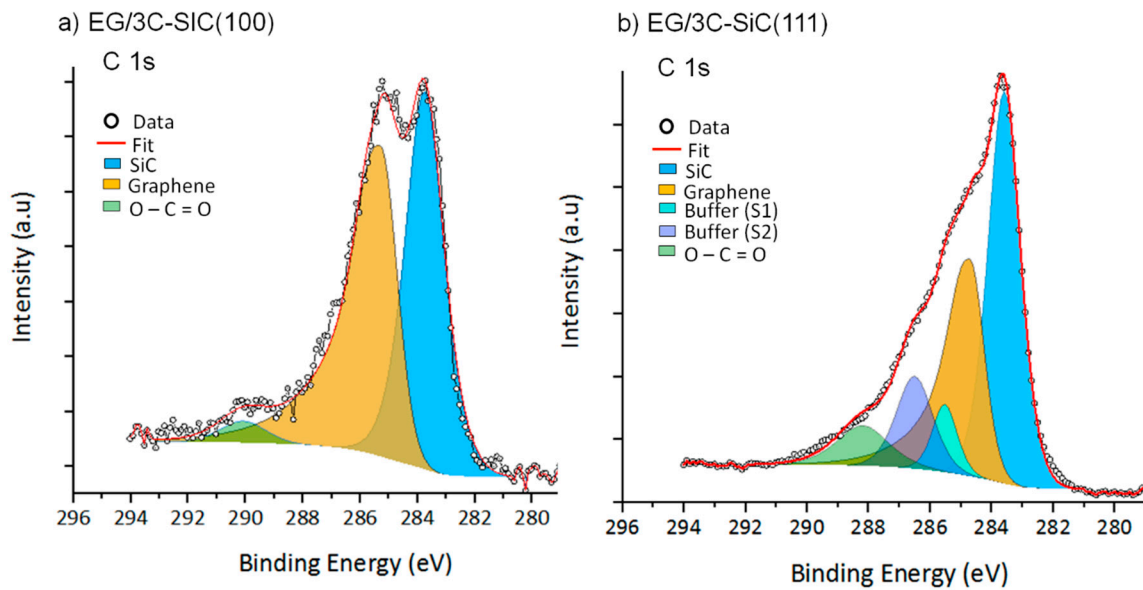
Figure 11. XPS C 1s core-level spectrum for (**a**) EG/3C-SiC (100) and (**b**) EG/3C-SiC (111). Buffer layer components are visible for EG/3C-SiC (111). Reprinted with permission from Reference [21]. Copyright (2020) American Chemical Society.

Graphene layers formed by thermal decomposition on 3C-SiC(111) are Bernal stacked as observed from scanning tunneling microscopy (STM) with a $(6\sqrt{3} \times 6\sqrt{3})$ rotated 30° construction at the interface similar to the EG on SiC(0001) [86]. On the other hand, the epi-layers on 3C-SiC(100) are rotated ±15° with respect to the substrate from LEED measurements by Ouerghi et al. [105]. Graphene formed by alloy-mediated graphitization on 3C-SiC(100) and 3C-SiC(111) are turbostratic, as observed from Raman spectroscopy [21].

The band structure and electronic properties of EG/3C-SiC(111) determined using ARPES showed linear band dispersion *K* point of the Brillouin zone with the E_F ~500 meV above the E_D indicating n-type monolayer graphene with doping of 10^{13} cm^{-2} [19,66]. The n-type doping is also in agreement with the DFT calculations [21]. Aristov et al. [16] determined the linear band dispersion for EG/3C-SiC(100) using ARPES with the E_F ~250 meV above E_D, which indicated n-type doping. The absence of the buffer layer in EG on 3C-SiC(100) resulted in a weak interaction with the substrate, as evident from E_F closer to E_D compared to EG on 3C-SiC(111) [16].

Transport measurements of EG/3C-SiC were first obtained using field-effect transistor (FET) -based measurements by Moon et al. [80] and Kang et al. using EG formed by thermal decomposition [20]. However, as mentioned in Section 3.3, these measurements are dependent on geometry and electrostatics, and are influenced by the substrate as well as the graphene that has an issue of inconsistent coverage over the substrate [61,102]. In addition, Pradeepkumar et al. reported that the EG grown on 3C-SiC on Si wafers are prone to severe 3C-SiC/Si interface degradation and the lack of large scale continuity of EG over 3C-SiC [106,107]. The prior attempts by Moon et al. and Kang et al. did not address these limitations. The alloy-mediated graphitization using 3C-SiC synthesized on highly-resistive Si wafers from Reference [21] overcame the interface degradation and continuous graphene coverage issues and enabled the large scale transport properties of EG using vdP Hall effect measurements, as given below.

The vdP transport measurements on EG from Reference [21] indicated that the EG-substrate interaction dominates the charge transport within EG. The graphene is strongly p-type doped (carrier concentration ~10^{13} cm^{-2}, mobility ~80 cm$^2\cdot$V$^{-1}\cdot$s^{-1} in EG/3C-SiC(100)) as a result of the EG-substrate interaction, which comprises of silicates (charge transfer from EG into the silicates) produced at the interface by the alloy-mediated synthesis. The buffer layer presence in EG/3C-SiC (111) reduces the charge transfer and improve the mobility almost five times compared to EG/3C-SiC(100) at a value of

330 $cm^2 \cdot V^{-1} \cdot s^{-1}$ and carrier concentration of 10^{12} cm^{-2} (p-type). The effect of interface silicates on the charge transport of EG on (100) and (111) 3C-SiC are in agreement with DFT calculations [21].

The transport measurements on EG also indicated that, within the observed diffusion regime (mean free path 3–10 nm), the grain sizes (<100 nm) and the number of graphene layers has no effect on the charge transport of EG. Further support to the lack of correlation of the grain sizes with the EG charge transport characteristics can also be found in the work by Ouerghi et al. [9,10]. A domain size of about 1 μm for EG/3C-SiC(111) was reported for the EG at a sheet carrier concentration of ~2 × 10^{13} cm^{-2} via the linear dispersion of DOS [66]—a value in line with the carrier concentration of EG/3C-SiC(111) from Reference [21] with grain sizes <100 nm.

4.2. Effect of Epitaxial Graphene-Ambient Interaction

The surface of EG is sensitive to a range of gases present in the ambient air [7–12]. Early on, researchers realized that adsorbed atoms or molecules on a graphene device could modify the channel conductivity. Schedin et al. [108] utilized this property to create a detector with sensitivity to very low concentrations of NH_3, NO_2, H_2O_2, and CO_2. Yet, graphene is relatively sensitive to all adsorbed molecules, and, hence, a requirement on building any sensor requires the ability to discriminate the target molecule from the background. An additional implication is that the surface of a graphene sample must be prepared to mitigate the effects of adsorbed molecules on transport properties. For example, heating the sample to temperatures ~400 °C in ultra-high vacuum (UHV) results in a clean, usable surface [109].

In a similar vein, Panchal et al. prepared a reproducible graphene surface to study the effects of adsorbed gases on work function and electrical properties. This led to several important findings. First, there are a range of molecules in the ambient (O_2, H_2O, and NO_2), which act as p-type dopants and reduces the n-type sheet charge density of graphene. Yet, there are other unidentified atmospheric contaminants, which also act as p-type dopants. It was suggested that some candidates are N_2O_4, CO_2, and various hydrocarbons. Lastly, it was shown that, for more than one graphene layer, the effect on conductivity was less, and it was proposed this was due to charge screening of the outermost layer. First-principles modeling indicates that the physical mechanism of the doping compensation (for H_2O, NH_3, CO, NO_2, and NO) and is due to charge transfer [110] from graphene to the molecule when the lowest unoccupied molecular orbital is below the Dirac point.

The polarity of the Si-face SiC gives rise to high hydrophilicity, which is relatively unchanged with the addition of a graphene monolayer [111]. Graphene's response to water and changes in the environment are strongly thickness dependent with a monolayer on Si-face being most sensitive to water adsorption than the bilayer or tri-layer graphene [5,112,113].

Yet, the understanding of the exact H_2O doping mechanism is not as well-understood since chemical processes may be involved. Sidorov et al. noted that, upon ambient exposure at 300 K, both the MEG and MLG on SiC(000$\bar{1}$) typically exhibit p-type conduction, 4.5 × 10^{14} cm^{-2} (Figure 12). The p-type doping is due to the ambient adsorbed film containing water vapour (H_2O), O_2, and NO_2 on the exposed surface [5,114]. The Dirac energy of the graphene lies near the redox potential of dissolved oxygen, which causes the surface charge transfer from graphene into the film (water/oxygen redox couple) and results in compensation of the n-type sheet density [2,5,46,114,115]. In addition, the conductivity state of vacuum annealed EG on SiC(000$\bar{1}$) is n-type (Figure 10b) [112,114]. This n-type conductivity was related to the work function considerations and E_F pinning at the state related to dangling bonds, as discussed in Section 4.1.3 [5]. Yet, we now know that the pseudo charge effect induced by substrate hexagonality dominates the graphene charge state.
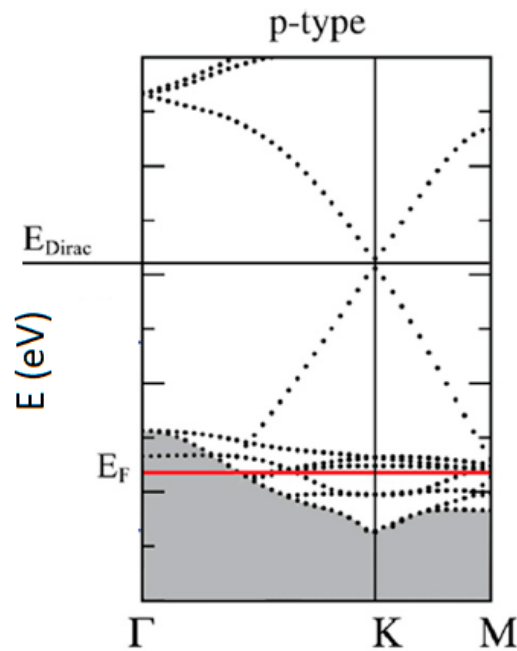
Figure 12. P-type doping of graphene upon the ambient exposure at 300 K. The p-type doping correspond to depletion of 4.5×10^{14} electrons/cm^{-2}. Adapted with permission from Reference [5]. Copyright (2012) AIP Publishing.

Knight et al. exposed monolayer EG on SiC(0001) to different inert gases and performed in-situ, contactless majority free charge carrier determination using terahertz-frequency optical Hall effect measurements [2]. The transport properties of graphene are also sensitive to other adsorbed gas molecules N_2O_4, CO_2, and hydrocarbons [2,5,114,116–118]. The mechanism of ambient doping is described as ambient-exposed graphene forms a thin film of water containing dissolved CO_2 that reacts with water forming H^+ ions. The oxygen in the water film reacts with H^+ ions to form additional water molecules, and electrons are removed from the graphene by p-doping the graphene. This doping is reversible and does not depend on the type of inert gas [2].

4.3. Effect of Epitaxial Graphene-Contact Metal Interaction

Since electronic transport measurements involve making metal contacts, understanding the influence of metal contacts on the transport of EG is also a concern [3]. The work function difference between graphene and a metal induces doping in graphene since the Fermi levels must equilibrate [3].

Since the E_F of freestanding graphene meets the E_D, the adsorption of metal can significantly alter its electronic properties [3], as the DOS of graphene at Dirac point is much lower than that of the metal. A tiny amount of charge transfer shifts the E_F significantly [25,33,34] as it is reported that 0.01 electrons per carbon atom would shift the E_F by 470 meV. The charge transfer creates a dipole layer at the graphene-metal interface with ΔV potential. The value of ΔV depends on the strength of the metal-graphene interaction. Even a weak interaction can cause a large shift in the E_F away from the E_D [3,119].

Khomyakov et al. [119] used DFT to characterize the adsorption of graphene on various metals and found graphene interacts more strongly to Ni, Co, Ti, and Pd (chemisorption). The chemisorption involves hybridization between graphene p_z and metal d-states that cause an opening of a band gap in the graphene. In the case of chemisorption, the band structure is disturbed, and the doping is estimated from the difference of work function between the graphene covered with metal and metal-free graphene. In the case of Ni, Co, Ti, and Pd, the graphene is n-type doped [119]. Physisorption, e.g., interaction with metals such as Ag, Al, Cu, Au, and Pt, involves only weak binding to graphene. Therefore, the electronic structure is preserved. In the case of physisorption, the electrons transfer from the

graphene to the metal, which causes the E_F to move closer to the E_D—and the hole doping is estimated from the change. At an equilibrium distance from the metal, the graphene is reported to be p-doped on Au and Pt and n-doped on Al, Ag, and Cu. Khomyakov et al. also reported that the graphene is doped n-type when the metal work function <5.4 eV, while it is p-type when the work function is >5.4 eV [119].

Using femtosecond laser-patterned microstructures (resist free, defect-free method), Nath et al. [120] studied the graphene-metal interactions on EG synthesized on 6H-SiC(0001) via thermal decomposition. They found that the nickel does not form bonds with EG on SiC in contrast to the Ni-C formation in chemical vapour deposition (CVD) grown graphene on metals due to the absence of defect sites [119]. However, it was shown that the contact resistance (R_C) of Ni to EG with resistance residue under the contact is an order of magnitude greater than the intrinsic quantum-limited R_C, which proposes the requirement for both end-contacts as well as a residue-free graphene–metal interface (which can form resistive $NiCO_3$) as requirements to obtain quantum-limited contact resistance [120].

DeJarld et al. [121] calculated the work functions of a number of high purity noble metals such as Cr, Cu, Rh, Ni, and Pt, and rare earth metals such as Pr, Eu, Er, Yb, and Y, in contact with MLG, using Kelvin Probe Force Microscopy. The metals were deposited under manufacturing-like conditions and Au (and its published work function) was used as the standard. The work functions were compared to published values for the other metals measured under careful, i.e., UHV, conditions. For the noble metals, a comparison showed Cr, Cu, and Rh had higher work functions (~0.5 eV) than expected and Ni and Pt were lower than expected (also ~0.5 eV). The low work function rare earth metal set were all affected, to various extents, by oxygen in the ambient and/or reactions to graphene rendering most unusable. The most stable rare earth was Yb, even though protection from the ambient was strongly recommended.

Yang et al. [122] demonstrated that the e-beam evaporated Ni on CVD graphene caused the EG work function to be 0.34 eV below the Ni work function. This resulted in electron transfer from graphene to Ni, which makes the graphene underneath the metal contact p-type.

4.4. Mobility and Sheet Carrier Concentration: Power-Law Relationship

A power-law relationship of mobility and sheet carrier concentration was demonstrated by several research groups for both EG on SiC and EG on 3C-SiC [4,21,25,57,59,123]. Tedesco et al. [56] described the functional power-law relationship between increasing mobility and decreasing carrier density as an intrinsic property of EG. The general power-law behaviour of mobility and sheet carrier concentration indicate that the tunability of graphene transport properties is constrained.

In Reference [21], the authors of this review demonstrate that the mobility versus sheet carrier concentration values for EG/SiC(0001) from Reference [56], and EG/3C-SiC can be fitted with good confidence using the same power law, which demonstrates a common conductivity of ~3 ± 1 (e^2/h) close to the minimum quantum conductivity of graphene (Figure 13). Note that the grain sizes of EG/SiC(0001) are at least 100 nm and more [124–126] whereas the EG/3C-SiC is smaller, which indicates that grain sizes do not determine the transport properties of EG [21].

In addition, Reference [21] demonstrated that the charge transport in EG/3C-SiC is dominated by the EG-substrate interaction resulting in p-type graphene due to a charge transfer from the EG into the interface silicates. The substrate interaction is stronger in EG/3C-SiC (100) and smaller in the case of EG/3C-SiC(111) due to the presence of a buffer layer in between EG and the substrate, which screens the charge transfer up to an extent. Figure 13 also indicates the different power-law nature of C-face EG from that of the Si-face EG and EG on 3C-SiC, which is due to distinct levels of EG-substrate interaction, according to Norimatsu et al. [11]. This was confirmed by Pradeepkumar et al. [21].
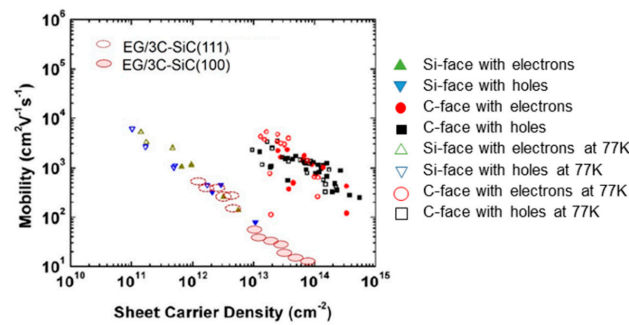
Figure 13. Mobility and sheet carrier density for EG on 3C-SiC/Si combined with those of monolayer EG on the Si-face of 4H-SiC and 6H-SiC substrates at 300 and 77 K from Tedesco et al. [36]. Reprinted with permission from Reference [21]. Copyright (2020) American Chemical Society.

4.5. Temperature-Dependent Transport: Scattering Mechanisms

Temperature-dependent Hall effect measurements in EG/SiC and 3C-SiC are crucial to investigate the charge transport as it provides information on the scattering mechanisms. This section summarizes the temperature-dependent transport properties of EG on Si-face SiC, EG on C-face SiC, and EG on 3C-SiC.

In general, Hwang et al. [93] reported that the carrier scattering mechanism dominant in MLG (on SiO_2) is Coulomb scattering by randomly charged impurities at the graphene-substrate interface, as also reported by Chen et al. [127]. The same group determined the typical random charged impurity concentration to be $\sim 10^{12}$ cm^2 and suggested that, by reducing this impurity concentration to $\sim 10^{10}$ cm^2 range, it should lead to a significant increase in the EG mobility. The charge transport in graphene dominated by the charged impurities in the substrate can be theoretically described by the Drude-Boltzmann model [93], which is valid only in the high-density regime [128]. The Fermi temperature of graphene is about 1300 K for n$\sim 10^{12}$ cm^2, which indicates no temperature dependence of the MLG conductivity arising from charged impurity scattering within a 0–300 K temperature range in agreement with the experimental observation of graphene flakes [93].

In contrast to the graphene flake results, MLG on Si-face SiC shows a strong temperature dependence of mobility and resistivity, as shown in Figure 14 [83,123,129]. At carrier concentrations away from the charge neutrality point (above 10^{11} cm^{-2}), the mobility decreases with increasing the temperature and the resistivity increases [123]. A remote phonon scattering originating from the SiC substrate including the buffer layer and the C-Si bonds at the interface was reported as the reason for the strong temperature dependence of mobility and resistivity, and the limitation of both properties at high temperatures [26,123,130,131]. Tedesco et al. [56] reported that the suppression of conductivity in high temperatures in the case of monolayer or bilayer Si-face EG is due to the scattering from the point defects present in the interfacial layer.
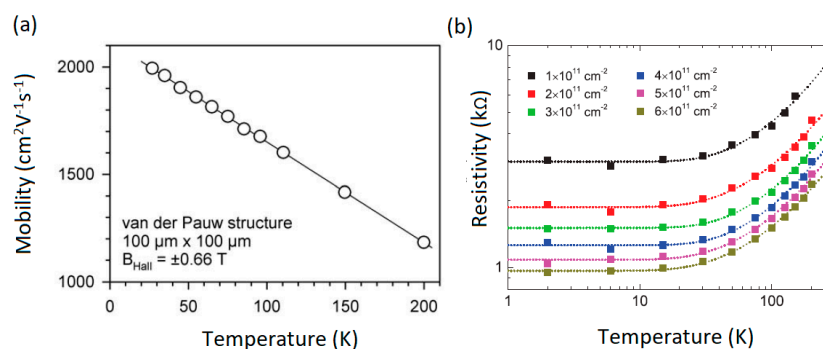

Figure 14. (**a**) Temperature dependent mobility of MLG on SiC (0001). Reprinted with permission from Reference [26]. Copyright (2009) Springer Nature. (**b**) Temperature dependent resistivity of MLG on SiC (0001). Reprinted with permission from Reference [123].

Figure 15 indicates the sheet resistance of rotationally disordered MEG (~10 layers) formed on SiC(000$\bar{1}$) [132], which indicates that the sheet resistance remains nearly stable within 0–300 K. This has been related to the weak substrate interaction of EG on the C-face SiC [11]. The mobility, in this case, does not significantly depend on temperature [8]. The phonon scattering is suppressed, and the scattering from impurities is weak.
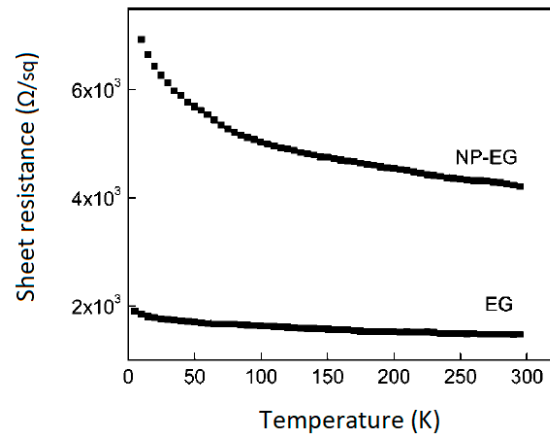

Figure 15. Temperature dependent sheet resistance of EG on SiC(000$\bar{1}$) and nitrophenyl functionalized graphene (NP-EG). Reprinted with permission from Reference [132]. Copyright (2009) American Chemical Society.

Figure 16 shows mobility versus temperature for EG/3C-SiC substrates [21]. The mobility of EG/3C-SiC (100) shows only a weak temperature dependence, slowly increasing after 200 K and reaching a value of ~30 $cm^2 \cdot V^{-1} \cdot s^{-1}$ at 300 K. This indicates charge impurity scattering. The weak temperature dependence of the mobility of EG/3C-SiC(100) is consistent with Reference [83] for EG on SiC, and is attributed to the absence of the buffer layer. In the case of EG/3C-SiC(111), the mobility shows a sharp increase after 200 K up to a value of ~375 $cm^2 \cdot V^{-1} \cdot s^{-1}$ at 250 K, which, again, indicates charge impurity scattering, and then a decrease to ~330 $cm^2 \cdot V^{-1} \cdot s^{-1}$ at 300 K. The negative temperature dependence of mobility for the EG/3C-SiC(111) above 250 K has been related to scattering at the buffer layer in EG on 6H-SiC [133]. At low temperatures, the charge impurity scattering is dominated [56,127] and, since the temperature is increased, the scattering decreases [25]. In addition, the constant value of conductivity (~3 ± 1 (e^2/h)) obtained for EG/3C-SiC also indicates that the charge impurity scattering at the interface dominates the transport [21].
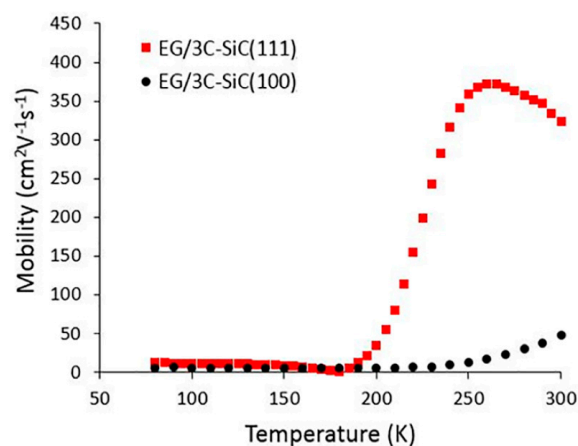

Figure 16. Temperature dependent mobility between 80 and 300 K for (100) and (111) EG/3C-SiC. Reprinted from Reference [21]. Copyright (2020) American Chemical Society.

5. Fine-Tuning of Transport Properties

Epitaxial graphene on SiC and 3C-SiC suffers from strong intrinsic n-type doping. The substrate-induced n-type doping in EG/SiC and EG/3C-SiC translates into the shift in the E_F, away from the E_D, such that the ambipolar properties of graphene cannot be exploited [79]. The substrate interaction causes larger charge density and lower mobility with strong temperature dependence when compared to freestanding graphene. Some of these issues can be compensated by tuning of the transport properties using different methods discussed in the following section.

5.1. Intercalation

Intercalation has been performed via different elements such as hydrogen [21,75,77,81,134], oxygen [78], fluorine [135], gold [136], and magnesium [43]. The monolayer graphene formed after intercalation of buffer layer on SiC (0001) is called quasi-free-standing monolayer graphene (QFMLG). Riedl et al. [134] produced QFMLG by annealing the buffer layer on Si-face SiC(0001) in atmospheric pressure H_2. The XPS C 1s and Si 2p spectra demonstrated that H saturate the Si dangling bonds and decouples the buffer layer by forming a monolayer graphene [134]. Buffer layer decoupling in EG on 3C-SiC (111) via H-intercalation has also been demonstrated [21,76].

The QFMLG on SiC (0001) films measured by ARPES are generally p-type doped [75] (see Figure 17). As discussed in Section 4.1.1, Mammadov et al. and Ristein et al. determined that the p-type conduction of QFMLG is caused by the spontaneous polarization of the SiC [75,81]. QFMLG layers formed on semi-insulating 4H-SiC (0001) indicated a hole concentration of 8.6×10^{12} cm^{-2} (stronger spontaneous polarization of 4H-SiC) extracted from the Fermi surface measurement [75] at E_F 340 meV below the E_D, whereas the QFMLG on 6H-SiC (0001) exhibits a p-type carrier concentration of 5.5×10^{12} cm^{-2} with E_F 300 meV below the E_D. The Fermi velocity was measured to be 0.98×10^6 ms^{-1} [33,75].
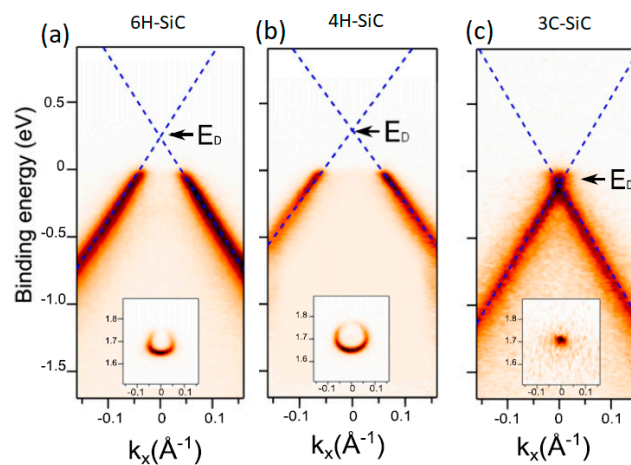

Figure 17. ARPES band structure of QFMLG formed on (**a**) 6H SiC, (**b**) 4H-SiC, and (**c**) 3C-SiC. Reprinted with permission from Reference [75]. Copyright (2014) IOP Publishing Ltd.

Speck et al. demonstrated that the mobility of QFMLG showed reduced temperature dependence compared with an as-grown MLG, which indicates reduced scattering from the underlying SiC (see Figure 18). The mobility of MLG falls by more than 50% when the temperature is increased from 25 K to 300 K whereas the change in mobility is only ~ 10% for the QFMLG across the same temperature range (samples indicated constant carrier concentration across the entire temperature range). The weak temperature dependence of mobility, approaching the behavior exhibited by flakes (see Section 4.5) signifies QFMLG is effectively decoupled from substrate compared to MLG [129]. Furthermore, for T greater than 290 K, the mobility of QFMLG are generally 3–5 times larger than EG before H-intercalation (Figure 18). The production of quasi-free-standing bilayer graphene by H-intercalation of MLG has also been achieved [77,137]. Reference [77] reported H-intercalated BLG

with a p-type carrier concentration of 10^{12} cm^{-2} with E_F 230 meV below the E_D. The Fermi velocity was measured to be 1.04×10^6 ms^{-1}.
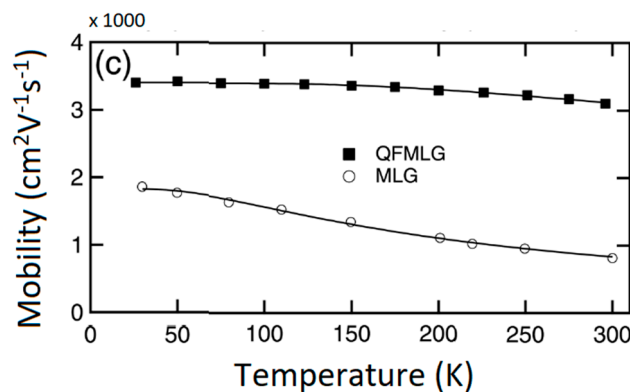

Figure 18. Temperature dependent mobility of QFMLG ($p = 5.7 \times 10^{12}$ cm^{-2}) and MLG (10^{13} cm^{-2}). Reprinted with permission from Reference [129]. Copyright (2011) AIP Publishing.

In contrast to the p-type polarization doping of QFMLG on bulk SiC substrates, the ARPES data of QFMLG on 3C-SiC (111) by H-intercalation reported slight n-type doping (see Figure 17c). This is due to the absence of spontaneous polarization in 3C-SiC [75]. The n-type doping density of about 10^{12} cm^{-2} was estimated, which was related to the residual defects at the interface [76]. Pradeepkumar et al. reported that the p-type transport properties of EG on 3C-SiC (111) did not improve after decoupling the buffer layer, which confirms that the interface silicates dominate the transport properties in this instance.

The intercalation process has also attempted via an oxidation process for EG on SiC (0001). Mathieu et al. [78] demonstrated that, through an oxidation process, the oxygen saturates Si dangling bonds and breaks some Si–C bonds of the buffer layer. In this case, the buffer layer is only partially decoupled, and the resulting sample had molecular oxygen intercalated between carbon layers with a ($\sqrt{3} \times \sqrt{3}$) rotated 30° pattern as observed with µLEED. The same group also demonstrated the possibility to tune the charge density modulation in the graphene by controlling the oxidation parameters. The starting sample had an n-type sheet charge of 1.4×10^{13} cm^{-2} corresponding to E_F of 500 meV below E_D. After the first O-intercalation step, the sheet density changed to 4.6×10^{12} cm^{-2} (n-type) and E_F of 300 meV. The second O-intercalation step yielded 1.9×10^{12} cm^{-2} (n-type) and E_F of 200 meV. Quasi-free-standing bilayer graphene (QFSBLG) with p-type doping of 10^{13} cm^{-2} was achieved by Oliveira Jr et al. via oxygen intercalation by annealing the monolayer graphene on SiC(0001) at 600 °C in the air [138].

The most advanced intercalation may be magnesium intercalation of monolayer EG on SiC (0001) creating QFSBLG [43]. For this case, ARPES measurements demonstrate a very high n-type concentration of 2×10^{14} cm^{-2} at an E_F of 720 meV above E_D and the creation of a band gap of 0.36 eV. The Fermi velocity was measured to be 0.97×10^6 ms^{-1}, which is only slightly different from MLG. This may indicate that the graphene lattice is only slightly perturbed by the magnesium intercalant.

Wong et al. [135] obtained a charge-neutral QFSG on SiC (0001) using fluorine from a fluorinated fullerene source, which was stable under ambient conditions, whereas resistant to temperatures up to 1200 °C. Gierz et al. [136] demonstrated buffer-layer decoupling using gold intercalation of EG on SiC (0001). The formation of an n-doped or a p-doped graphene layer can be controlled by varying the gold coverage about one-third or one monolayer, respectively.

5.2. Functionalization of EG

Controlling the transport properties via surface functionalization makes use of charge compensation from surface adsorption or attachments [139]. Coletti et al. demonstrated that the intrinsic n-type doping of EG on SiC (0001) can be compensated by functionalizing graphene (non-covalent) with an electron

acceptor called as tetrafluorotetracyanoquinodimethane (F4-TCNQ) [79]. Surface transfer doping results in charge transfer from graphene into the doping molecule reducing the sheet density. A 0.8-nm-thick layer of F4-TCNQ on monolayer EG resulted in near charge neutrality, i.e., $E_F = E_D$, Figure 19. For a bilayer sample, the band gap more than doubled, moving from about 100 meV to 250 meV [79] with the E_F shifted into the band gap. Yet, both the compensation and band gap widening saturated near 0.8 nm, which indicated that there may be limitations with this approach. An increase of mobility with decreasing carrier density was seen in the F4-TCNQ doped samples by Jobst et al. [55]. When the carrier density is decreased, the mobility limited by the electron interaction with substrate phonons rises substantially (up to 29,000 cm^2·V^{-1}·s^{-1} at 25 K), and Shubnikov–de Haas oscillations and the graphene-like quantum Hall effect are observed [55]. The F4-TCNQ experiments demonstrate that the effects of the substrate interaction can be mitigated by reducing the sheet density, and the quantum Hall effect and pseudo-relativistic physics and linear band structure are possible in the epitaxial graphene.
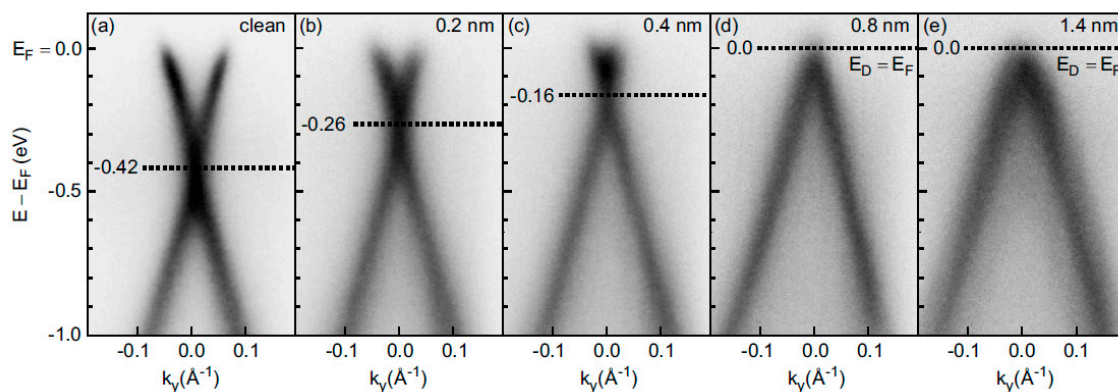

Figure 19. ARPES measured π bands for around K point for the Brillouin zone for (**a**) as-grown graphene monolayer on SiC (0001) (**b**–**e**) increasing amount of F4-TCNQ. Reprinted with permission from Reference [79].

Bekyarova et al. [132] studied the transport properties of nitrophenylfunctionalized EG (NP-EG formed on the C-face SiC) and suggested that it changes the graphene from near-metallic to semiconducting (see Figure 15) [132].

Other interesting work by Lartsev et al. [140] demonstrate charge neutrality (10^{11} cm^{-2}) and p-doping (5×10^{12} cm^{-2}) by reversible tuning of carrier density via high electrostatic potential gating with ions produced by corona discharge in initially strongly n-doped EG/SiC devices. In this case, the ions deposited on the dielectric layer induce a surface charge density on the graphene. The corona effect is reversible and, depending on the ionic charge, both p-doping and n-doping are possible. The method is utilized in graphene applications such as quantum resistance metrology where specific fixed doping is required.

Peles-Lemli et al. [141] used DFT calculations to investigate the graphene interactions with the adsorbed alkali metal ions such as Li$^+$, Na$^+$, and K$^+$ for the applications of graphene-based chemical sensors. In the presence of an external electric field, the positively charged ions get closer to the graphene inducing excess charge transfer from the graphene surface to the metal ions, causing negative charges on the ions and removal of the ions from the surface. Ludbrook et al. [142] demonstrated first direct observation of superconductivity (critical temperature of 5.9 K) for monolayer graphene formed on 6H-SiC (0001) decorated with a layer of lithium atoms at a low temperature, which caused an enhanced electron-phonon coupling.

5.3. Top-Gate Graphene Field-Effect Transistors

The ability to control the graphene transport properties via an external voltage is the heart of future electronics [29]. Graphene field-effect transistors show ambipolar field-effect due to its unique electronic band structure with a zero band gap [58]. Under a gate voltage control, charge

carriers in graphene can be tuned continuously between electrons and holes with the Fermi level crossing the Dirac point [143]. Charge carriers can be tuned up to 10^{13} cm^{-2} with mobilities over 15,000 cm^2·V^{-1}·s^{-1} at 300 K [29]. The mobilities depend on temperature weakly, which indicates charge impurity scattering and, therefore, the gate control may be able to improve those numbers further, even up to ≈100,000 cm^2·V^{-1}·s^{-1} [58].

The first report of epitaxial graphene field-effect transistors (EG FETs) patterned on a single epitaxial graphene chip both on the SiC (0001) and SiC (000$\bar{1}$) was made in 2008 [60]. Figure 20 demonstrates the Id-Vg characteristics of the C-face and Si-face transistors. The results from this work show that the gate-controlled tuning can lead to mobility as high as 5000 cm^2·V^{-1}·s^{-1} on the C-face, and an on/off ratio up to 7 on the Si-face SiC. Moon et al. [144] measured the first small-signal radio-frequency (RF) performance of EG FETs on 6H-SiC(0001). Lin et al. [145] fabricated high-speed graphene RF FETs on 4H-SiC (0001) and obtained a cutoff frequency of 100 GHz for a gate length of 240 nm. He et al. [146] revealed the RF performance of bilayer GFETs up to 200 °C. Yu et al. [147] formed a QFSBLG FET on 4H-SiC (0001), (100-nm gate length) with an intrinsic current gain cutoff frequency 407 GHz. Hwang et al. [148] demonstrated the first top-gated graphene nanoribbon FETs of 10 nm width on 6H-SiC (0001). The results exhibited exceptionally high drive currents (for fast switching) and opening of a substantial band gap of 0.14 eV. Bianco et al. [149] determined the detection of terahertz radiation at room temperature using antenna-coupled EG FETs on SiC, which introduced the potential of plasmonic detectors using epitaxial graphene on silicon carbide.
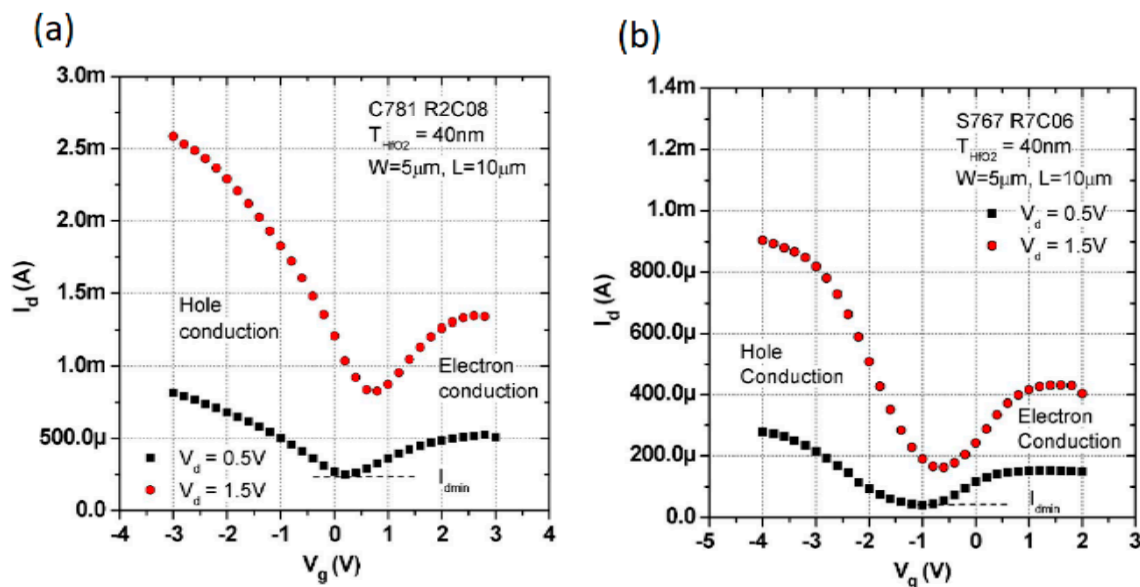

Figure 20. Id−Vg characteristics for FET fabricated on (**a**) MEG on SiC (000$\bar{1}$) transistor for 0.5 V and 1.5 V drain voltages, (**b**) EG on SiC (0001) transistor for two drain voltages. Reprinted with permission from Reference [60]. Copyright (2008) Institute of Electrical and Electronics Engineers.

Additionally, the gate control in FET fabricated on bilayer EG enables us to selectively adjust the carrier concentration in each layer and induce a band gap in bilayer graphene. Ohta et al. demonstrated that, by doping the bilayer of graphene, the band gap of 200 meV could be achieved [34]. Alternatively, Zhang et al. showed the band gap of up to 250 meV is achievable by varying the electric field and by using an external gate control. Zhou et al. [45] reported a substrate-induced energy gap of 260 meV [37].

Moon et al. demonstrated the first ambipolar behavior of wafer-scale EG FET on 3C-SiC(111)/Si substrates formed via thermal decomposition (see Figure 21) [80]. A comparison of the graphene FETs fabricated on Si(110) and Si(111) substrates were reported by Kang et al. [20]. The graphene FETs on Si(111) exhibited higher channel currents, which is an order of magnitude larger than those

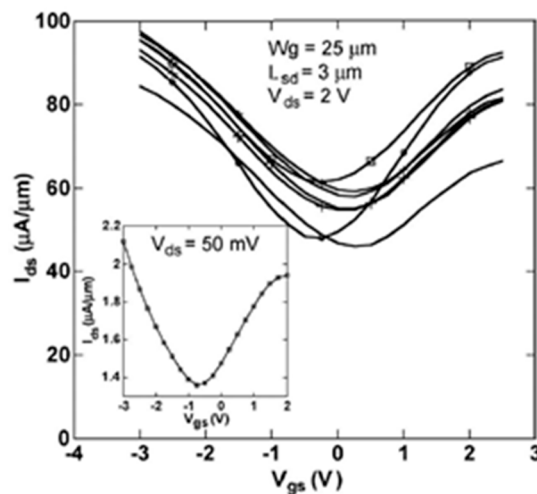on Si(110) substrates. However, the measurements indicated the presence of a large amount of gate-leakage current.

Figure 21. Ambipolar field-effect transistor on Si (111) substrates. Reprinted with permission from Reference [80]. Copyright (2010) Institute of Electrical and Electronics Engineers.

Fabrication of graphene FETs involves the challenges of selecting an appropriate gate insulator and controlling its thickness [150]. Generally, the oxides such as SiO_2, HfO_2, Al_2O_3, and Y_2O_3 are used as the gate dielectrics, but these tend to become amorphous with scaling and interactions with the graphene can occur, which makes the high-quality defect-free interface formation difficult [150–152]. Hexagonal boron nitride (h-BN) forms a weak van der Waals interaction with the graphene (lattice mismatch only 2% [153]) and has been utilized as an ideal insulator for the graphene FET formation [151]. Due to the lower value of a dielectric constant (k~4), h-BN is usually combined with a high k-dielectric layer such as Y_2O_3 formed via atomic layer deposition on h-BN [154]. The scaling (~1.3 nm) of h-BN results in excessive gate leakage current within the FET. To overcome this, Illarionov et al. [150] utilized epitaxial calcium fluoride of ~2 nm thickness as a gate insulator with low leakage current and on/off ratio up to 10^7. Furthermore, the epitaxial growth of graphene-h-BN heterostructures on copper via chemical vapor deposition has been demonstrated by Geng et al. [155].

6. Conclusions

Epitaxial graphene is a practical approach for electronics and photonic applications thanks to its wafer-scale integration compatibility [5]. The knowledge and the control of electronic and transport properties of epitaxial graphene are crucial for graphene-based electronic and photonics applications.

This work has reviewed the impact of different interactions the epitaxial graphene makes with its surroundings, such as substrate, ambient, and metal contacts. The review concluded that the electronic and charge transport properties of EG on both SiC and Si substrates are always dominated by the interfaces between graphene and its environment. Within the diffusion regime, the grain sizes do not affect carrier transport in EG. The sheet carrier concentration and the mobility of graphene follow a power-law dependence, which is universal for the substrate-supported graphene. Lastly, different methods to tune the electronic and transport properties of EG are discussed, which points out that the control of the charge transfer/doping in EG is directly linked for engineering the graphene interfaces. Hence, it is critical for the integration of graphene into future micro-electronic or nano-electronic devices.

References

1. Motta, N.; Iacopi, F.; Coletti, C. *Growing Graphene on Semiconductors*; Pan Stanford: Singapore, 2017.
2. Knight, S.; Hofmann, T.; Bouhafs, C.; Armakavicius, N.; Kühne, P.; Stanishev, V.; Ivanov, I.G.; Yakimova, R.; Wimer, S.; Schubert, M.; et al. In-situ terahertz optical Hall effect measurements of ambient effects on free charge carrier properties of epitaxial graphene. *Sci. Rep.* **2017**, *7*, 1–8. [CrossRef]
3. Giovannetti, G.; Khomyakov, P.; Brocks, G.; Karpan, V.M.; Van den Brink, J.; Kelly, P.J. Doping graphene with metal contacts. *Phys. Rev. Lett.* **2008**, *101*, 026803. [CrossRef]
4. Berger, C.; Song, Z.; Li, T.; Li, X.; Ogbazghi, A.Y.; Feng, R.; Dai, Z.; Marchenkov, A.N.; Conrad, E.H.; First, P.N.; et al. Ultrathin epitaxial graphite: 2D electron gas properties and a route toward graphene-based nanoelectronics. *J. Phys. Chem. B* **2004**, *108*, 19912–19916. [CrossRef]
5. Sidorov, A.N.; Gaskill, K.; Buongiorno Nardelli, M.; Tedesco, J.L.; Myers-Ward, R.L.; Eddy, C.R., Jr.; Jayasekera, T.; Kim, K.W.; Jayasingha, R.; Sherehiy, A.; et al. Charge transfer equilibria in ambient-exposed epitaxial graphene on (0001̄) 6H-SiC. *J. Appl. Phys.* **2012**, *111*, 113706. [CrossRef]
6. Nishi, Y. Semiconductor Interfaces and Their Implications to VLSI Device Reliability. In *Control of Semiconductor Interfaces*; Elsevier: Amsterdam, The Netherlands, 1994; pp. 9–12.
7. Rhoderick, E. Surfaces and Interfaces in Semiconductor Technology. In *Physics and Contemporary Needs*; Springer: Berlin/Heidelberg, Germany, 1978; pp. 3–28.
8. Berger, C.; Song, Z.; Li, X.; Wu, X.; Brown, N.; Naud, C.; Mayou, D.; Li, T.; Hass, J.; Marchenkov, A.N.; et al. Electronic confinement and coherence in patterned epitaxial graphene. *Science* **2006**, *312*, 1191–1196. [CrossRef] [PubMed]
9. Hannon, J.; Copel, M.; Tromp, R. Direct Measurement of the Growth Mode of Graphene on SiC (0001) and SiC (000 1̄). *Phys. Rev. Lett.* **2011**, *107*, 166101. [CrossRef] [PubMed]
10. Seyller, T.; Bostwick, A.; Emtsev, K.; Horn, K.; Ley, L.; McChesney, J.; Ohta, T.; Riley, J.D.; Rotenberg, E.; Speck, F. Epitaxial graphene: A new material. *Phys. Status Solidi B* **2008**, *245*, 1436–1446. [CrossRef]
11. Norimatsu, W.; Kusunoki, M. Structural features of epitaxial graphene on SiC {0 0 0 1} surfaces. *J. Phys. D Appl. Phys.* **2014**, *47*, 094017. [CrossRef]
12. Hass, J.; Varchon, F.; Millán-Otoya, J.; Sprinkle, M.; de Heer, W.; Berger, C.; First, P.; Magaud, L.; Conrad, E. Rotational stacking and its electronic effects on graphene films grown on 4H-SiC (0001̄). *arXiv* **2007**, arXiv:0706.2134.
13. Hite, J.K.; Twigg, M.E.; Tedesco, J.L.; Friedman, A.L.; Myers-Ward, R.L.; Eddy, C.R., Jr.; Gaskill, D.K. Epitaxial graphene nucleation on C-face silicon carbide. *Nano Lett.* **2011**, *11*, 1190–1194. [CrossRef] [PubMed]
14. Lin, Y.-M.; Dimitrakopoulos, C.; Farmer, D.B.; Han, S.-J.; Wu, Y.; Zhu, W.; Gaskill, D.K.; Tedesco, J.L.; Myers-Ward, R.L.; Eddy, C.R., Jr.; et al. Multicarrier transport in epitaxial multilayer graphene. *Appl. Phys. Lett.* **2010**, *97*, 112107. [CrossRef]
15. Wu, X.; Hu, Y.; Ruan, M.; Madiomanana, N.K.; Hankinson, J.; Sprinkle, M.; Berger, C.; de Heer, W.A. Half integer quantum Hall effect in high mobility single layer epitaxial graphene. *Appl. Phys. Lett.* **2009**, *95*, 223108. [CrossRef]
16. Aristov, V.Y.; Urbanik, G.; Kummer, K.; Vyalikh, D.V.; Molodtsova, O.V.; Preobrajenski, A.B.; Zakharov, A.A.; Hess, C.; Hänke, T.; Buchner, B.; et al. Graphene synthesis on cubic SiC/Si wafers. Perspectives for mass production of graphene-based electronic devices. *Nano Lett.* **2010**, *10*, 992–995. [CrossRef] [PubMed]
17. Suemitsu, M.; Fukidome, H. Epitaxial graphene on silicon substrates. *J. Phys. D Appl. Phys.* **2010**, *43*, 374012. [CrossRef]
18. Gupta, B.; Notarianni, M.; Mishra, N.; Shafiei, M.; Iacopi, F.; Motta, N. Evolution of epitaxial graphene layers on 3C SiC/Si (1 1 1) as a function of annealing temperature in UHV. *Carbon* **2014**, *68*, 563–572. [CrossRef]
19. Ouerghi, A.; Marangolo, M.; Belkhou, R.; El Moussaoui, S.; Silly, M.; Eddrief, M.; Largeau, L.; Portail, M.; Fain, B.; Sirotti, F. Epitaxial graphene on 3C-SiC (111) pseudosubstrate: Structural and electronic properties. *Phys. Rev. B* **2010**, *82*, 125445. [CrossRef]

20. Kang, H.-C.; Karasawa, H.; Miyamoto, Y.; Handa, H.; Fukidome, H.; Suemitsu, T.; Suemitsu, M.; Otsuji, T. Epitaxial graphene top-gate FETs on silicon substrates. *Solid State Electron.* **2010**, *54*, 1071–1075. [CrossRef]

21. Pradeepkumar, A.; Amjadipour, M.; Mishra, N.; Liu, C.; Fuhrer, M.S.; Bendavid, A.; Isa, F.; Zielinski, M.; Sirikumara, H.I.; Jayasekera, T.; et al. p-type Epitaxial Graphene on Cubic Silicon Carbide on Silicon for Integrated Silicon Technologies. *ACS Appl. Nano Mater.* **2019**. [CrossRef]

22. Wallace, P.R. The band theory of graphite. *Phys. Rev.* **1947**, *71*, 622. [CrossRef]

23. Hass, J.; Varchon, F.; Millan-Otoya, J.-E.; Sprinkle, M.; Sharma, N.; de Heer, W.A.; Berger, C.; First, P.N.; Magaud, L.; Conrad, E.H. Why multilayer graphene on 4 H− SiC (000 1) behaves like a single sheet of graphene. *Phys. Rev. Lett.* **2008**, *100*, 125504. [CrossRef] [PubMed]

24. Neto, A.H.C.; Guinea, F.; Peres, N.M.R.; Novoselov, K.S.; Geim, A.K. The electronic properties of graphene. *Rev. Mod. Phys.* **2009**, *81*, 109. [CrossRef]

25. Zhu, W.; Perebeinos, V.; Freitag, M.; Avouris, P. Carrier scattering, mobilities, and electrostatic potential in monolayer, bilayer, and trilayer graphene. *Phys. Rev. B* **2009**, *80*, 235402. [CrossRef]

26. Emtsev, K.V.; Bostwick, A.; Horn, K.; Jobst, J.; Kellogg, G.L.; Ley, L.; McChesney, J.L.; Ohta, T.; Reshanov, S.A.; Röhrl, J.; et al. Towards wafer-size graphene layers by atmospheric pressure graphitization of silicon carbide. *Nat. Mater.* **2009**, *8*, 203–207. [CrossRef] [PubMed]

27. Nakada, K.; Fujita, M.; Dresselhaus, G.; Dresselhaus, M.S. Edge state in graphene ribbons: Nanometer size effect and edge shape dependence. *Phys. Rev. B* **1996**, *54*, 17954. [CrossRef] [PubMed]

28. Zhang, Y.; Tan, Y.-W.; Stormer, H.L.; Kim, P. Experimental observation of the quantum Hall effect and Berry's phase in graphene. *Nature* **2005**, *438*, 201–204. [CrossRef]

29. Novoselov, K.S.; Geim, A.K.; Morozov, S.V.; Jiang, D.; Zhang, Y.; Dubonos, S.V.; Grigorieva, I.V.; Firsov, A.A. Electric field effect in atomically thin carbon films. *Science* **2004**, *306*, 666–669. [CrossRef] [PubMed]

30. Mattausch, A.; Pankratov, O. Ab initio study of graphene on SiC. *Phys. Rev. Lett.* **2007**, *99*, 076802. [CrossRef]

31. Varchon, F.; Feng, R.; Hass, J.; Li, X.; Nguyen, B.N.; Naud, C.; Mallet, P.; Veuillen, J.-Y.; Berger, C.; Conrad, E.H.; et al. Electronic structure of epitaxial graphene layers on SiC: Effect of the substrate. *Phys. Rev. Lett.* **2007**, *99*, 126805. [CrossRef]

32. Bostwick, A.; Ohta, T.; Seyller, T.; Horn, K.; Rotenberg, E. Quasiparticle dynamics in graphene. *Nat. Phys.* **2007**, *3*, 36–40. [CrossRef]

33. Ohta, T.; Bostwick, A.; McChesney, J.L.; Seyller, T.; Horn, K.; Rotenberg, E. Interlayer interaction and electronic screening in multilayer graphene investigated with angle-resolved photoemission spectroscopy. *Phys. Rev. Lett.* **2007**, *98*, 206802. [CrossRef]

34. Ohta, T.; Bostwick, A.; Seyller, T.; Horn, K.; Rotenberg, E. Controlling the electronic structure of bilayer graphene. *Science* **2006**, *313*, 951–954. [CrossRef]

35. Sprinkle, S.M.; Siegel, D.; Hu, Y.; Hicks, J.; Tejeda, A.; Taleb-Ibrahimi, A.; le Fèvre, P.; Bertran, F.; Vizzini, S.; Enriquez, H.; et al. First direct observation of a nearly ideal graphene band structure. *Phys. Rev. Lett.* **2009**, *103*, 226803. [CrossRef] [PubMed]

36. Starke, U.; Riedl, C. Epitaxial graphene on SiC (0001) and: From surface reconstructions to carbon electronics. *J. Phys. Condens. Matter.* **2009**, *21*, 134016. [CrossRef]

37. Zhou, S.Y.; Gweon, G.-H.; Fedorov, A.; de First, P.; de Heer, W.; Lee, D.-H.; Guinea, F.; Neto, A.C.; Lanzara, A. Substrate-induced bandgap opening in epitaxial graphene. *Nat. Mater.* **2007**, *6*, 770–775. [CrossRef] [PubMed]

38. Bychkov, Y.A.; Martinez, G. Magnetoplasmon excitations in graphene for filling factors $\nu \leq 6$. *Phys. Rev. B* **2008**, *77*, 125417. [CrossRef]

39. Davydov, S.Y. Estimations of the Fermi Velocity and Effective Mass in Epitaxial Graphene and Carbyne. *Tech. Phys. Lett.* **2019**, *45*, 650–652. [CrossRef]

40. McCann, E.; Fal'ko, V.I. Landau-level degeneracy and quantum Hall effect in a graphite bilayer. *Phys. Rev. Lett.* **2006**, *96*, 086805. [CrossRef]

41. Sarma, S.D.; Hwang, E.; Rossi, E. Theory of carrier transport in bilayer graphene. *Phys. Rev. B* **2010**, *81*, 161407. [CrossRef]

42. McCann, E.; Koshino, M. The electronic properties of bilayer graphene. *Rep. Prog. Phys.* **2013**, *76*, 056503. [CrossRef]

43. Grubišić-Čabo, A.; Kotsakidis, J.C.; Yin, Y.; Tadich, A.; Haldon, M.; Solari, S.; di Bernardo, I.; Daniels, K.M.; Riley, J.; Huwald, E.; et al. Magnesium-intercalated graphene on SiC: Highly n-doped air-stable bilayer graphene at extreme displacement fields. *Mesoscale Nanoscale Phys.* **2020**, arXiv:2005.02670.

44. Novoselov, K.S.; McCann, E.; Morozov, S.; Fal'ko, V.I.; Katsnelson, M.; Zeitler, U.; Jiang, D.; Schedin, F.; Geim, A. Unconventional quantum Hall effect and Berry's phase of 2π in bilayer graphene. *Nature Phys.* **2006**, *2*, 177–180. [CrossRef]

45. Zhang, Y.; Tang, T.-T.; Girit, C.; Hao, Z.; Martin, M.C.; Zettl, A.; Crommie, M.F.; Shen, Y.R.; Wang, F. Direct observation of a widely tunable bandgap in bilayer graphene. *Nature* **2009**, *459*, 820–823. [CrossRef]

46. Escobedo-Cousin, E.; Vassilevski, K.; Hopf, T.; Wright, N.; O'Neill, A.; Horsfall, A.; Goss, J.; Cumpson, P. Local solid phase growth of few-layer graphene on silicon carbide from nickel silicide supersaturated with carbon. *J. Appl. Phys.* **2013**, *113*, 114309. [CrossRef]

47. Jayasekera, T.; Kim, K.; Nardelli, M.B. Electronic and Structural Properties of Turbostratic Epitaxial Graphene on the 6H-SiC (000-1) Surface. *Mater. Sci. Forum* **2012**, *717–720*, 595–600. [CrossRef]

48. Siegel, D.A.; Hwang, C.; Fedorov, A.V.; Lanzara, A. Quasifreestanding multilayer graphene films on the carbon face of SiC. *Phys. Rev. B* **2010**, *81*, 241417. [CrossRef]

49. Orlita, M.; Faugeras, C.; Plochocka, P.; Neugebauer, P.; Martinez, G.; Maude, D.K.; Barra, A.-L.; Sprinkle, M.; Berger, C.; de Heer, W.A.; et al. Approaching the Dirac point in high-mobility multilayer epitaxial graphene. *Phys. Rev. Lett.* **2008**, *101*, 267601. [CrossRef]

50. Miller, D.L.; Kubista, K.D.; Rutter, G.M.; Ruan, M.; de Heer, W.A.; First, P.N.; Stroscio, J.A. Observing the quantization of zero mass carriers in graphene. *Science* **2009**, *324*, 924–927. [CrossRef]

51. Ji, S.-H.; Hannon, J.; Tromp, R.; Perebeinos, V.; Tersoff, J.; Ross, F. Atomic-scale transport in epitaxial graphene. *Nat. Mater.* **2012**, *11*, 114–119. [CrossRef]

52. Yakes, M.K.; Gunlycke, D.; Tedesco, J.L.; Campbell, P.M.; Myers-Ward, R.L.; Eddy, C.R., Jr.; Gaskill, D.K.; Sheehan, P.E.; Laracuente, A.R. Conductance anisotropy in epitaxial graphene sheets generated by substrate interactions. *Nano Lett.* **2010**, *10*, 1559–1562. [CrossRef]

53. Janssen, T.J.B.M.; Tzalenchuk, A.; Lara-Avila, S.; Kubatkin, S.; Fal'ko, V.I. Quantum resistance metrology using graphene. *Rep. Prog. Phys.* **2013**, *76*, 104501. [CrossRef]

54. Kruskopf, M.; Pakdehi, D.M.; Pierz, K.; Wundrack, S.; Stosch, R.; Dziomba, T.; Götz, M.; Baringhaus, J.; Aprojanz, J.; Tegenkamp, C.; et al. Comeback of epitaxial graphene for electronics: Large-area growth of bilayer-free graphene on SiC. *2D Mater.* **2016**, *3*, 041002. [CrossRef]

55. Jobst, J.; Waldmann, D.; Speck, F.; Hirner, R.; Maude, D.K.; Seyller, T.; Weber, H.B. Transport properties of high-quality epitaxial graphene on 6H-SiC (0001). *Solid State Commun.* **2011**, *151*, 1061–1064. [CrossRef]

56. Tedesco, J.L.; VanMil, B.L.; Myers-Ward, R.L.; McCrate, J.M.; Kitt, S.A.; Campbell, P.M.; Jernigan, G.G.; Culbertson, J.C.; Eddy, C.R., Jr.; Gaskill, D.K. Hall effect mobility of epitaxial graphene grown on silicon carbide. *Appl. Phys. Lett.* **2009**, *95*, 122102. [CrossRef]

57. van der Pauw, L.J. A method of measuring specific resistivity and Hall effect of discs of arbitrary shape. *Philips Res. Rep.* **1958**, *13*, 1–9.

58. Geim, A.K.; Novoselov, K.S. The Rise of Graphene. In *Nanoscience and Technology: A Collection of Reviews from Nature Journals*; World Scientific: Singapore, 2010; pp. 11–19.

59. Lin, Y.-M.; Farmer, D.B.; Jenkins, K.A.; Wu, Y.; Tedesco, J.L.; Myers-Ward, R.L.; Myers-Ward, C.R.; Gaskill, D.K.; Dimitrakopoulos, C.; Avouris, P. Enhanced performance in epitaxial graphene FETs with optimized channel morphology. *IEEE Electron. Device Lett.* **2011**, *32*, 1343–1345. [CrossRef]

60. Kedzierski, J.; Hsu, P.-L.; Healey, P.; Wyatt, P.W.; Keast, C.L.; Sprinkle, M.; Berger, C.; de Heer, W.A. Epitaxial graphene transistors on SiC substrates. *IEEE T Electron. Dev.* **2008**, *55*, 2078–2085. [CrossRef]

61. Ytterdal, T.; Cheng, Y.; Fjeld, T.O. *Device Modeling for Analog 801 and RF CMOS Circuit Design*; John Wiley & Sons: Hoboken, NJ, USA, 2003.

62. Röhrl, J.; Hundhausen, M.; Speck, F.; Seyller, T. Strain and charge in epitaxial graphene on silicon carbide studied by raman spectroscopy. *Mater. Sci. Forum* **2010**, *645–648*, 603–606. [CrossRef]

63. Thomsen, C.; Reich, S. Double resonant Raman scattering in graphite. *Phys. Rev. Lett.* **2000**, *85*, 5214–5217. [CrossRef]

64. Ferrari, A.C.; Meyer, J.; Scardaci, V.; Casiraghi, C.; Lazzeri, M.; Mauri, F.; Piscanec, S.; Jiang, D.; Novoselov, K.; Roth, S.; et al. Raman spectrum of graphene and graphene layers. *Phys. Rev. Lett.* **2006**, *97*, 187401. [CrossRef]

65. Das, A.; Pisana, S.; Chakraborty, B.; Piscanec, S.; Saha, S.K.; Waghmare, U.V.; Novoselov, K.S.; Krishnamurthy, H.R.; Geim, A.K.; Ferrari, A.C.; et al. Monitoring dopants by Raman scattering in an electrochemically top-gated graphene transistor. *Nat. Nanotechnol.* **2008**, *3*, 210–215. [CrossRef]

66. Ouerghi, A.; Kahouli, A.; Lucot, D.; Portail, M.; Travers, L.; Gierak, J.; Penuelas, J.; Jegou, P.; Shukla, A.; Chassagne, T.; et al. Epitaxial graphene on cubic SiC (111)/Si (111) substrate. *Appl. Phys. Lett.* **2010**, *96*, 191910. [CrossRef]

67. Mueller, N.S.; Heeg, S.; Alvarez, M.P.; Kusch, P.; Wasserroth, S.; Clark, N.; Schedin, F.; Parthenios, J.; Papagelis, K.; Galiotis, C.; et al. Evaluating arbitrary strain configurations and doping in graphene with Raman spectroscopy. *2D Mater.* **2017**, *5*, 015016. [CrossRef]

68. Verhagen, T.; Drogowska, K.; Kalbac, M.; Vejpravova, J. Temperature-induced strain and doping in monolayer and bilayer isotopically labeled graphene. *Phys. Rev. B* **2015**, *92*, 125437. [CrossRef]

69. Shtepliuk, I.; Ivanov, I.G.; Pliatsikas, N.; Iakimov, T.; Jamnig, A.; Sarakinos, K.; Yakimova, R. Probing the uniformity of silver-doped epitaxial graphene by micro-Raman mapping. *Phys. B Condens. Matter* **2020**, *580*, 411751. [CrossRef]

70. Shtepliuk, I.; Ivanov, I.G.; Iakimov, T.; Yakimova, R.; Kakanakova-Georgieva, A.; Fiorenza, P.; Giannazzo, F. Raman probing of hydrogen-intercalated graphene on Si-face 4H-SiC. *Mater. Sci. Semicond. Process.* **2019**, *96*, 145–152. [CrossRef]

71. Pisana, S.; Lazzeri, M.; Casiraghi, C.; Novoselov, K.S.; Geim, A.K.; Ferrari, A.C.; Mauri, F. Breakdown of the adiabatic Born–Oppenheimer approximation in graphene. *Nat. Mater.* **2007**, *6*, 198–201. [CrossRef] [PubMed]

72. Sun, D.; Wu, Z.-K.; Divin, C.; Li, X.; Berger, C.; de Heer, W.A.; First, P.N.; Norris, T.B. Ultrafast relaxation of excited Dirac fermions in epitaxial graphene using optical differential transmission spectroscopy. *Phys. Rev. Lett.* **2008**, *101*, 157402. [CrossRef] [PubMed]

73. Hofmann, T.; Boosalis, A.; Kühne, P.; Herzinger, C.; Woollam, J.A.; Gaskill, D.; Tedesco, J.; Schubert, M. Hole-channel conductivity in epitaxial graphene determined by terahertz optical-Hall effect and midinfrared ellipsometry. *Appl. Phys. Lett.* **2011**, *98*, 041906. [CrossRef]

74. Armakavicius, N.; Bouhafs, C.; Stanishev, V.; Kühne, P.; Yakimova, R.; Knight, S.; Hofmann, T.; Schubert, M.; Darakchieva, V. Cavity-enhanced optical Hall effect in epitaxial graphene detected at terahertz frequencies. *Appl. Surf. Sci.* **2017**, *421*, 357–360. [CrossRef]

75. Mammadov, S.; Ristein, J.; Koch, R.J.; Ostler, M.; Raidel, C.; Wanke, M.; Vasiliauskas, R.; Yakimova, R.; Seyller, T. Polarization doping of graphene on silicon carbide. *2D Mater.* **2014**, *1*, 035003. [CrossRef]

76. Coletti, C.; Emtsev, K.V.; Zakharov, A.A.; Ouisse, T.; Chaussende, D.; Starke, U. Large area quasi-free standing monolayer graphene on 3C-SiC (111). *Appl. Phys. Lett.* **2011**, *99*, 081904. [CrossRef]

77. Grubišić-Čabo, A.; Monash University, Melbourne, Victoria, Australia. Personal communication, 2020.

78. Mathieu, C.; Lalmi, B.; Menteş, T.; Pallecchi, E.; Locatelli, A.; Latil, S.; Belkhou, R.; Ouerghi, A. Effect of oxygen adsorption on the local properties of epitaxial graphene on SiC (0001). *Phys. Rev. B* **2012**, *86*, 035435. [CrossRef]

79. Coletti, C.; Riedl, C.; Lee, D.S.; Krauss, B.; Patthey, L.; von Klitzing, K.; Smet, J.H.; Starke, U. Charge neutrality and band-gap tuning of epitaxial graphene on SiC by molecular doping. *Phys. Rev. B* **2010**, *81*, 235401. [CrossRef]

80. Moon, J.; Curtis, D.; Bui, S.; Marshall, T.; Wheeler, D.; Valles, I.; Kim, S.; Wang, E.; Weng, X.; Fanton, M. Top-gated graphene field-effect transistors using graphene on Si (111) wafers. *IEEE Electron. Device Lett.* **2010**, *31*, 1193–1195. [CrossRef]

81. Ristein, J.; Mammadov, S.; Seyller, T. Origin of doping in quasi-free-standing graphene on silicon carbide. *Phys. Rev. Lett.* **2012**, *108*, 246104. [CrossRef] [PubMed]

82. Kopylov, S.; Tzalenchuk, A.; Kubatkin, S.; Fal'ko, V.I. Charge transfer between epitaxial graphene and silicon carbide. *Appl. Phys. Lett.* **2010**, *97*, 112109. [CrossRef]

83. Speck, F.; Ostler, M.; Röhrl, J.; Jobst, J.; Waldmann, D.; Hundhausen, M.; Ley, L.; Weber, H.B.; Seyller, T. Quasi-freestanding graphene on SiC (0001). *Mater. Sci. Forum* **2010**, *645–648*, 629–632. [CrossRef]

84. De Heer, W.A.; Berger, C.; Wu, X.; Sprinkle, M.; Hu, Y.; Ruan, M.; Stroscio, J.A.; First, P.N.; Haddon, R.; Piot, B.; et al. Epitaxial graphene electronic structure and transport. *J. Phys. D Appl. Phys.* **2010**, *43*, 374007. [CrossRef]

85. Van Bommel, A.; Crombeen, J.; Van Tooren, A. LEED and Auger electron observations of the SiC (0001) surface. *Surf. Sci.* **1975**, *48*, 463–472. [CrossRef]

86. Emtsev, K.; Speck, F.; Seyller, T.; Ley, L.; Riley, J.D. Interaction, growth, and ordering of epitaxial graphene on SiC {0001} surfaces: A comparative photoelectron spectroscopy study. *Phys. Rev. B* **2008**, *77*, 155303. [CrossRef]

87. Seubert, A.; Bernhardt, J.; Nerding, M.; Starke, U.; Heinz, K. In situ surface phases and silicon-adatom geometry of the (2×2) C structure on 6H-SiC (0001⁻). *Surf. Sci.* **2000**, *454*, 45–48. [CrossRef]

88. Malard, L.; Pimenta, M.; Dresselhaus, G.; Dresselhaus, M. Raman spectroscopy in graphene. *Phys. Rep.* **2009**, *473*, 51–87. [CrossRef]

89. De Heer, W.A.; Berger, C.; Wu, X.; First, P.N.; Conrad, E.H.; Li, X.; Li, T.; Sprinkle, M.; Hass, J.; Sadowski, M.L.; et al. Epitaxial graphene. *Solid State Commun.* **2007**, *143*, 92–100. [CrossRef]

90. First, P.N.; de Heer, W.A.; Seyller, T.; Berger, C.; Stroscio, J.A.; Moon, J.-S. Epitaxial graphenes on silicon carbide. *MRS Bull.* **2010**, *35*, 296–305. [CrossRef]

91. Orlita, M.; Faugeras, C.; Grill, R.; Wysmolek, A.; Strupinski, W.; Berger, C.; de Heer, W.A.; Martinez, G.; Potemski, M. Carrier scattering from dynamical magnetoconductivity in quasineutral epitaxial graphene. *Phys. Rev. Lett.* **2011**, *107*, 216603. [CrossRef] [PubMed]

92. Lebedev, A.A.; Agrinskaya, N.V.; Beresovets, V.A.; Kozub, V.I.; Lebedev, S.P.; Sitnikova, A.A. Low temperature transport properties of multigraphene structures on 6H-SiC obtained by thermal graphitization: Evidences of a presence of nearly perfect graphene layer. *arXiv Preprint*, 2012; arXiv:1212.4272.

93. Hwang, E.; Adam, S.; Sarma, S.D. Carrier transport in two-dimensional graphene layers. *Phys. Rev. Lett.* **2007**, *98*, 186806. [CrossRef]

94. Jernigan, G.G.; VanMil, B.L.; Tedesco, J.L.; Tischler, J.G.; Glaser, E.R.; Davidson, A., III; Campbell, P.M.; Gaskill, D.K. Comparison of epitaxial graphene on Si-face and C-face 4H SiC formed by ultrahigh vacuum and RF furnace production. *Nano Lett.* **2009**, *9*, 2605–2609. [CrossRef]

95. Hu, Y.; Ruan, M.; Guo, Z.; Dong, R.; Palmer, J.; Hankinson, J.; Berger, C.; de Heer, W.A. Structured epitaxial graphene: Growth and properties. *J. Phys. D Appl. Phys.* **2012**, *45*, 154010. [CrossRef]

96. Dimitrakopoulos, C.; Grill, A.; McArdle, T.J.; Liu, Z.; Wisnieff, R.; Antoniadis, D.A. Effect of SiC wafer miscut angle on the morphology and Hall mobility of epitaxially grown graphene. *Appl. Phys. Lett.* **2011**, *98*, 222105. [CrossRef]

97. Gaskill, D.K. Epitaxial Graphene. In *Handbook of Crystal Growth*; Elsevier: Amsterdam, The Netherlands, 2015; pp. 755–783.

98. Novoselov, K.S.; Geim, A.K.; Morozov, S.; Jiang, D.; Katsnelson, M.I.; Grigorieva, I.; Dubonos, S.; Firsov, A.A. Two-dimensional gas of massless Dirac fermions in graphene. *Nature* **2005**, *438*, 197–200. [CrossRef] [PubMed]

99. Elias, D.; Gorbachev, R.; Mayorov, A.; Morozov, S.; Zhukov, A.; Blake, P.; Ponomarenko, L.; Grigorieva, I.; Novoselov, K.; Guinea, F.; et al. Dirac cones reshaped by interaction effects in suspended graphene. *Nat. Phys.* **2011**, *7*, 701–704. [CrossRef]

100. Mayorov, A.S.; Elias, D.C.; Mukhin, I.S.; Morozov, S.V.; Ponomarenko, L.A.; Novoselov, K.S.; Geim, A.; Gorbachev, R.V. How close can one approach the Dirac point in graphene experimentally? *Nano Lett.* **2012**, *12*, 4629–4634. [CrossRef]

101. Bolotin, K.I.; Sikes, K.J.; Jiang, Z.; Klima, M.; Fudenberg, G.; Hone, J.; Kim, P.; Stormer, H. Ultrahigh electron mobility in suspended graphene. *Solid State Commun.* **2008**, *146*, 351–355. [CrossRef]

102. Aristov, V.Y.; Molodtsova, O.V.; Chaika, A.N. Graphene synthesized on Cubic-SiC(001) in Ultrahigh Vacuum: Atomic and Electronic Structure and Transport Properties. In *Growing Graphene on Semiconductors*; Motta, N., Iacopi, F., Coletti, C., Eds.; Pan Stanford: Singapore, 2017; pp. 27–75.

103. Ago, H.; Ito, Y.; Mizuta, N.; Yoshida, K.; Hu, B.; Orofeo, C.M.; Tsuji, M.; Ikeda, K.-i.; Mizuno, S. Epitaxial chemical vapor deposition growth of single-layer graphene over cobalt film crystallized on sapphire. *ACS Nano* **2010**, *4*, 7407–7414. [CrossRef]

104. Fukidome, H.; Miyamoto, Y.; Handa, H.; Saito, E.; Suemitsu, M. Epitaxial growth processes of graphene on silicon substrates. *Jpn. J. Appl. Phys.* **2010**, *49*, 01AH03. [CrossRef]

105. Ouerghi, A.; Ridene, M.; Balan, A.; Belkhou, R.; Barbier, A.; Gogneau, N.; Portail, M.; Michon, A.; Latil, S.; Jegou, P.; et al. Sharp interface in epitaxial graphene layers on 3 C-SiC (100)/Si (100) wafers. *Phys. Rev. B* **2011**, *83*, 205429. [CrossRef]

106. Pradeepkumar, A.; Zielinski, M.; Bosi, M.; Verzellesi, G.; Gaskill, D.K.; Iacopi, F. Electrical leakage phenomenon in heteroepitaxial cubic silicon carbide on silicon. *J. Appl. Phys.* **2018**, *123*, 215103. [CrossRef]

107. Pradeepkumar, A.; Mishra, N.; Kermany, A.R.; Boeckl, J.J.; Hellerstedt, J.; Fuhrer, M.S.; Iacopi, F. Catastrophic degradation of the interface of epitaxial silicon carbide on silicon at high temperatures. *Appl. Phys. Lett.* **2016**, *109*, 011604. [CrossRef]

108. Schedin, F.; Geim, A.K.; Morozov, S.V.; Hill, E.; Blake, P.; Katsnelson, M.; Novoselov, K.S. Detection of individual gas molecules adsorbed on graphene. *Nat. Mater.* **2007**, *6*, 652–655. [CrossRef]

109. Kotsakidis, J.C.; Grubišić-Čabo, A.; Yin, Y.; Tadich, A.; Myers-Ward, R.L.; Dejarld, M.; Pavunny, S.P.; Currie, M.; Daniels, K.M.; Liu, C.; et al. Freestanding n-Doped Graphene via Intercalation of Calcium and Magnesium Into the Buffer Layer-SiC (0001) Interface. *arXiv Preprint*, 2020; arXiv:2004.01383.

110. Leenaerts, O.; Partoens, B.; Peeters, F. Adsorption of H_2O, NH_3, CO, NO_2, and NO on graphene: A first-principles study. *Phys. Rev. B* **2008**, *77*, 125416. [CrossRef]

111. Kazakova, O.; Panchal, V.; Burnett, T.L. Epitaxial graphene and graphene–based devices studied by electrical scanning probe microscopy. *Crystals* **2013**, *3*, 191–233. [CrossRef]

112. Giusca, C.E.; Panchal, V.; Munz, M.; Wheeler, V.D.; Nyakiti, L.O.; Myers-Ward, R.L.; Gaskill, D.K.; Kazakova, O. Water affinity to epitaxial graphene: The impact of layer thickness. *Adv. Mater. Interfaces* **2015**, *2*, 1500252. [CrossRef]

113. Munz, M.; Giusca, C.E.; Myers-Ward, R.L.; Gaskill, D.K.; Kazakova, O. Thickness-dependent hydrophobicity of epitaxial graphene. *Acs Nano* **2015**, *9*, 8401–8411. [CrossRef] [PubMed]

114. Panchal, V.; Giusca, C.E.; Lartsev, A.; Martin, N.A.; Cassidy, N.; Myers-Ward, R.L.; Gaskill, D.K.; Kazakova, O. Atmospheric doping effects in epitaxial graphene: Correlation of local and global electrical studies. *2D Mater.* **2016**, *3*, 015006. [CrossRef]

115. Yang, Y.; Brenner, K.; Murali, R. The influence of atmosphere on electrical transport in graphene. *Carbon* **2012**, *50*, 1727–1733. [CrossRef]

116. Pearce, R.; Iakimov, T.; Andersson, M.; Hultman, L.; Spetz, A.L.; Yakimova, R. Epitaxially grown graphene based gas sensors for ultra sensitive NO2 detection. *Sens. Actuators B Chem.* **2011**, *155*, 451–455. [CrossRef]

117. Kong, L.; Enders, A.; Rahman, T.S.; Dowben, P.A. Molecular adsorption on graphene. *J. Phys. Condens. Matter.* **2014**, *26*, 443001. [CrossRef]

118. Nomani, M.W.; Shishir, R.; Qazi, M.; Diwan, D.; Shields, V.; Spencer, M.; Tompa, G.S.; Sbrockey, N.M.; Koley, G. Highly sensitive and selective detection of NO2 using epitaxial graphene on 6H-SiC. *Sens. Actuators B Chem.* **2010**, *150*, 301–307. [CrossRef]

119. Khomyakov, P.; Giovannetti, G.; Rusu, P.; Brocks, G.; van den Brink, J.; Kelly, P.J. First-principles study of the interaction and charge transfer between graphene and metals. *Phys. Rev. B* **2009**, *79*, 195425. [CrossRef]

120. Nath, A.; Currie, M.; Boyd, A.K.; Wheeler, V.D.; Koehler, A.D.; Tadjer, M.J.; Robinson, Z.R.; Sridhara, K.; Hernandez, S.C.; Wollmershauser, J.A.; et al. In search of quantum-limited contact resistance: Understanding the intrinsic and extrinsic effects on the graphene—Metal interface. *2D Mater.* **2016**, *3*, 025013. [CrossRef]

121. DeJarld, M.; Campbell, P.M.; Friedman, A.L.; Currie, M.; Myers-Ward, R.L.; Boyd, A.K.; Rosenberg, S.G.; Pavunny, S.P.; Daniels, K.M.; Gaskill, D. Surface potential and thin film quality of low work function metals on epitaxial graphene. *Sci. Rep.* **2018**, *8*, 1–11. [CrossRef]

122. Yang, S.; Zhou, P.; Chen, L.; Sun, Q.; Wang, P.; Ding, S.; Jiang, A.; Zhang, D.W. Direct observation of the work function evolution of graphene-two-dimensional metal contacts. *J. Mater. Chem.* **2014**, *2*, 8042–8046. [CrossRef]

123. Tanabe, S.; Sekine, Y.; Kageshima, H.; Nagase, M.; Hibino, H. Carrier transport mechanism in graphene on SiC (0001). *Phys. Rev. B* **2011**, *84*, 115458. [CrossRef]

124. Daniels, K.M.; Jadidi, M.M.; Sushkov, A.B.; Nath, A.; Boyd, A.K.; Sridhara, K.; Drew, H.D.; Murphy, T.E.; Myers-Ward, R.L.; Gaskill, D.K. Narrow plasmon resonances enabled by quasi-freestanding bilayer epitaxial graphene. *2D Mater.* **2017**, *4*, 025034. [CrossRef]

125. Ohta, T.; El Gabaly, F.; Bostwick, A.; McChesney, J.L.; Emtsev, K.V.; Schmid, A.K.; Seyller, T.; Horn, K.; Rotenberg, E. Morphology of graphene thin film growth on SiC (0001). *New J. Phys.* **2008**, *10*, 023034. [CrossRef]

126. Hass, J.; Feng, R.; Li, T.; Li, X.; Zong, Z.; de Heer, W.; First, P.; Conrad, E.; Jeffrey, C.; Berger, C. Highly ordered graphene for two dimensional electronics. *Appl. Phys. Lett.* **2006**, *89*, 143106. [CrossRef]

127. Chen, J.-H.; Jang, C.; Adam, S.; Fuhrer, M.; Williams, E.D.; Ishigami, M. Charged-impurity scattering in graphene. *Nat. Phys.* **2008**, *4*, 377–381. [CrossRef]

128. Sarma, S.D.; Adam, S.; Hwang, E.; Rossi, E. Electronic transport in two-dimensional graphene. *Rev. Mod. Phys.* **2011**, *83*, 407. [CrossRef]

129. Speck, F.; Jobst, J.; Fromm, F.; Ostler, M.; Waldmann, D.; Hundhausen, M.; Weber, H.B.; Seyller, T. The quasi-free-standing nature of graphene on H-saturated SiC (0001). *Appl. Phys. Lett.* **2011**, *99*, 122106. [CrossRef]

130. Chen, J.-H.; Jang, C.; Xiao, S.; Ishigami, M.; Fuhrer, M.S. Intrinsic and extrinsic performance limits of graphene devices on SiO_2. *Nat. Nanotechnol.* **2008**, *3*, 206. [CrossRef] [PubMed]

131. Morozov, S.; Novoselov, K.; Katsnelson, M.; Schedin, F.; Elias, D.; Jaszczak, J.A.; Geim, A. Giant intrinsic carrier mobilities in graphene and its bilayer. *Phys. Rev. Lett.* **2008**, *100*, 016602. [CrossRef]

132. Bekyarova, E.; Itkis, M.E.; Ramesh, P.; Berger, C.; Sprinkle, M.; de Heer, W.A.; Haddon, R.C. Chemical modification of epitaxial graphene: Spontaneous grafting of aryl groups. *J. Am. Chem. Soc.* **2009**, *131*, 1336–1337. [CrossRef]

133. Giesbers, A.; Procházka, P.; Flipse, C. Surface phonon scattering in epitaxial graphene on 6 H-SiC. *Phys. Rev. B* **2013**, *87*, 195405. [CrossRef]

134. Riedl, C.; Coletti, C.; Iwasaki, T.; Zakharov, A.; Starke, U. Quasi-free-standing epitaxial graphene on SiC obtained by hydrogen intercalation. *Phys. Rev. Lett.* **2009**, *103*, 246804. [CrossRef]

135. Wong, S.L.; Huang, H.; Wang, Y.; Cao, L.; Qi, D.; Santoso, I.; Chen, W.; Wee, A.T.S. Quasi-free-standing epitaxial graphene on SiC (0001) by fluorine intercalation from a molecular source. *ACS Nano* **2011**, *5*, 7662–7668. [CrossRef]

136. Gierz, I.; Suzuki, T.; Weitz, R.T.; Lee, D.S.; Krauss, B.; Riedl, C.; Starke, U.; Höchst, H.; Smet, J.H.; Ast, C.R. Electronic decoupling of an epitaxial graphene monolayer by gold intercalation. *Phys. Rev. B* **2010**, *81*, 235408. [CrossRef]

137. Virojanadara, C.; Zakharov, A.; Yakimova, R.; Johansson, L.I. Buffer layer free large area bi-layer graphene on SiC (0 0 0 1). *Surf. Sci.* **2010**, *604*, L4–L7. [CrossRef]

138. Oliveira, M.H., Jr.; Schumann, T.; Fromm, F.; Koch, R.; Ostler, M.; Ramsteiner, M.; Seyller, T.; Lopes, J.M.J.; Riechert, H. Formation of high-quality quasi-free-standing bilayer graphene on SiC (0 0 0 1) by oxygen intercalation upon annealing in air. *Carbon* **2013**, *52*, 83–89. [CrossRef]

139. Joucken, F.; Henrard, L.; Lagoute, J. Electronic properties of chemically doped graphene. *Phys. Rev. Mater.* **2019**, *3*, 110301. [CrossRef]

140. Lartsev, A.; Yager, T.; Bergsten, T.; Tzalenchuk, A.; Janssen, T.M.; Yakimova, R.; Lara-Avila, S.; Kubatkin, S. Tuning carrier density across Dirac point in epitaxial graphene on SiC by corona discharge. *Appl. Phys. Lett.* **2014**, *105*, 063106. [CrossRef]

141. Peles-Lemli, B.; Kánnár, D.; Nie, J.C.; Li, H.; Kunsági-Máté, S. Some unexpected behavior of the adsorption of alkali metal ions onto the graphene surface under the effect of external electric field. *J. Phys. Chem. C* **2013**, *117*, 21509–21515. [CrossRef]

142. Ludbrook, B.; Levy, G.; Nigge, P.; Zonno, M.; Schneider, M.; Dvorak, D.; Veenstra, C.; Zhdanovich, S.; Wong, D.; Dosanjh, P.; et al. Evidence for superconductivity in Li-decorated monolayer graphene. *Proc. Natl. Acad. Sci. USA* **2015**, *112*, 11795–11799. [CrossRef]

143. Feng, T.; Xie, D.; Lin, Y.; Tian, H.; Zhao, H.; Ren, T.; Zhu, H. Unipolar to ambipolar conversion in graphene field-effect transistors. *Appl. Phys. Lett.* **2012**, *101*, 253505. [CrossRef]

144. Moon, J.; Curtis, D.; Hu, M.; Wong, D.; McGuire, C.; Campbell, P.; Jernigan, G.; Tedesco, J.; VanMil, B.; Myers-Ward, R.; et al. Epitaxial-graphene RF field-effect transistors on Si-face 6H-SiC substrates. *IEEE Electron. Device Lett.* **2009**, *30*, 650–652. [CrossRef]

145. Lin, Y.-M.; Dimitrakopoulos, C.; Jenkins, K.A.; Farmer, D.B.; Chiu, H.-Y.; Grill, A.; Avouris, P. 100-GHz transistors from wafer-scale epitaxial graphene. *Science* **2010**, *327*, 662. [CrossRef] [PubMed]

146. He, Z.; Yu, C.; Liu, Q.; Song, X.; Gao, X.; Guo, J.; Zhou, C.; Cai, S.; Feng, Z. High temperature RF performances of epitaxial bilayer graphene field-effect transistors on SiC substrate. *Carbon* **2020**, *164*, 435–441. [CrossRef]

147. Yu, C.; He, Z.; Li, J.; Song, X.; Liu, Q.; Cai, S.; Feng, Z. Quasi-free-standing bilayer epitaxial graphene field-effect transistors on 4H-SiC (0001) substrates. *Appl. Phys. Lett.* **2016**, *108*, 013102. [CrossRef]

148. Hwang, W.S.; Zhao, P.; Tahy, K.; Nyakiti, L.O.; Wheeler, V.D.; Myers-Ward, R.L.; Eddy, C.R., Jr.; Gaskill, D.K.; Robinson, J.A.; Haensch, W.; et al. Graphene nanoribbon field-effect transistors on wafer-scale epitaxial graphene on SiC substrates. *APL Mater.* **2015**, *3*, 011101. [CrossRef]

149. Bianco, F.; Perenzoni, D.; Convertino, D.; De Bonis, S.; Spirito, D.; Perenzoni, M.; Coletti, C.; Vitiello, M.; Tredicucci, A. Terahertz detection by epitaxial-graphene field-effect-transistors on silicon carbide. *Appl. Phys. Lett.* **2015**, *107*, 131104. [CrossRef]

150. Illarionov, Y.Y.; Banshchikov, A.G.; Polyushkin, D.K.; Wachter, S.; Knobloch, T.; Thesberg, M.; Mennel, L.; Paur, M.; Stöger-Pollach, M.; Steiger-Thirsfeld, A.; et al. Ultrathin calcium fluoride insulators for two-dimensional field-effect transistors. *Nat. Electron.* **2019**, *2*, 230–235. [CrossRef]

151. Giannazzo, F.; Schilirò, E.; Lo Nigro, R.; Roccaforte, F.; Yakimova, R. Atomic Layer Deposition of High-k Insulators on Epitaxial Graphene: A Review. *Appl. Sci.* **2020**, *10*, 2440. [CrossRef]

152. Sangwan, V.K.; Hersam, M.C. Electronic transport in two-dimensional materials. *Annu. Rev. Phys. Chem.* **2018**, *69*, 299–325. [CrossRef]

153. Liu, Z.; Ma, L.; Shi, G.; Zhou, W.; Gong, Y.; Lei, S.; Yang, X.; Zhang, J.; Yu, J.; Hackenberg, K.P.; et al. In-plane heterostructures of graphene and hexagonal boron nitride with controlled domain sizes. *Nat. Nanotechnol.* **2013**, *8*, 119. [CrossRef]

154. Takahashi, N.; Watanabe, K.; Taniguchi, T.; Nagashio, K. Atomic layer deposition of Y2O3 on h-BN for a gate stack in graphene FETs. *Nanotechnology* **2015**, *26*, 175708. [CrossRef]

155. Geng, D.; Dong, J.; Ang, L.K.; Ding, F.; Yang, H.Y. In situ epitaxial engineering of graphene and h-BN lateral heterostructure with a tunable morphology comprising h-BN domains. *NPG Asia Mater.* **2019**, *11*, 1–8. [CrossRef]